

A Hot Mess: The Rich and Complex Soft Emitting Regions Surrounding the Reflection Dominated Flaring Central Engine of Mrk 1239M. Z. BUHARIWALLA,¹ L. C. GALLO,¹ J. MAO,^{2,3} J. JIANG,⁴ L. K. POTHIER-BOGOSLOWSKI,¹ E. JÄRVELÄ,⁵ S. KOMOSSA,⁶ AND D. GRUPE⁷¹*Department of Astronomy and Physics, Saint Mary's University, 923 Robie Street, Halifax, NS B3H 3C3, Canada*²*Department of Astronomy, Tsinghua University, 30 Shuangqing Road, Beijing 100084, China*³*Department of Physics, Hiroshima University, 1-3-1 Kagamiyama, HigashiHiroshima, Hiroshima 739-8526, Japan*⁴*Institute of Astronomy, Madingley Road, Cambridge CB3 0HA, UK*⁵*Homer L. Dodge Department of Physics and Astronomy, The University of Oklahoma, 440 W. Brooks St., Norman, OK 73019, USA*⁶*Max-Planck-Institut für Radioastronomie, Auf dem Hügel 69, 53121, Bonn Germany*⁷*Department of Physics, Geology, and Engineering Technology Science Center, Northern Kentucky University, 1 Nunn Drive, Highland Heights, KY 41099*

(Received xxx yyy zzz; Revised xxx yyy zzz)

Submitted to ApJ

ABSTRACT

Previous X-ray works on Mrk 1239 have revealed a complex Narrow Line Seyfert 1 (NLS1) that exhibits substantial absorption and strong emission from both collisional (CIE) and photoionized (PIE) plasmas. Here, we report on deep-pointed observations with *XMM-Newton* and *NuSTAR*, along with *Swift* monitoring, to understand the 0.3 – 30 keV continuum emission and the central engine geometry. A strong X-ray flare, where the AGN brightens by a factor of five in ~ 30 ks, is captured between 4 – 30 keV and can be attributed to a brightening of the primary continuum. However, the lack of any variability below ~ 3 keV on long- or short-time scales requires complete absorption of the AGN continuum with a neutral medium of column density $\sim 10^{23.5} \text{ cm}^{-2}$. The timing and spectral properties are consistent with a blurred reflection interpretation for the primary emission. The variability and presence of a Compton hump disfavors ionized partial covering. The neutral absorber, if outflowing, could be crashing into the surrounding medium and ISM to produce the low-energy continuum and CIE. Scattered emission off the inner torus could produce the PIE. The intricate scenario is demanded by the data and highlights the complexity of the environment that is normally invisible when overwhelmed by the AGN continuum. Objects like Mrk 1239 serve as important sources for unveiling the interface between the AGN and host galaxy environments.

Keywords: galaxies: active – galaxies: nuclei – galaxies: individual: Mrk 1239 – X-rays: galaxies**1. INTRODUCTION**

According to the Unified Model (e.g. [Antonucci 1993](#), [Urry & Padovani 1995](#), [Urry 2003](#)), all active galactic nuclei (AGN) are fundamentally the same. They consist of a supermassive black hole (SMBH) surrounded by an accretion disc (e.g. [Shakura & Sunyaev 1973](#)), a broad line region (BLR) (e.g. [Peterson & Wandel 1999](#); [Peterson et al. 2004](#)), and a dusty torus (e.g. [Netzer 2013](#); [Peterson 1997](#)). These compo-

nents are thought to exist in all AGN, and the various AGN classifications indicate different viewing angles through the obscuring torus. Type I AGN offer a clear, unobstructed view of the accretion disc and BLR with low inclinations and low column densities. In contrast, Type II AGNs are thought to have much more edge on view through the obscuring torus ([Antonucci 1993](#)), effectively absorbing all the soft (less than 3 keV) photons emitted from the AGN.

In AGN, the primary X-ray source is considered to be the corona, a cloud of hot electrons located above the accretion disc that Compton-up scatter UV disc photons to higher energies ([Haardt & Maraschi 1993](#)). Some of these photons are emitted directly as the primary X-ray continuum, while

others are reflected by the accretion disc and surrounding material, producing reflection spectra (e.g. [George & Fabian 1991](#)). Photons reflected near the SMBH produce a blurred ionized spectrum due to the immense relativistic effects (e.g. [Tanaka et al. 1995](#); [Laor 1991](#); [Ballantyne et al. 2001](#); [Ross & Fabian 2005](#)), while photons reflected at larger distances produce narrow, near neutral emission features ([Nandra et al. 1997](#)). The hard X-ray spectra above 10 keV can be attributed to the primary continuum, Compton hump, synchrotron self-Comptonization (SSC) from radio jets ([Netzer 2013](#)) or any combination of these components.

AGN can shape their host galaxy by way of kinetic or radiative feedback ([Morganti 2017](#), and ref. therein). We see evidence of this in the M - σ relation, where the mass of the SMBH scales with the stellar velocity dispersion of the halo stars (e.g. [Gültekin et al. 2009](#)). Kinetic feedback is driven by radio jets shooting out of the central engine and interacting with the host galaxy (e.g. [Fabian 2012](#)). Radiative feedback is dominant when young nuclei are surrounded by cold neutral gas that can be radiatively driven away from the central engine (e.g. [Fabian 2012](#)). Depending on the Eddington ratio of the source and the column density of the obscuring cloud, clouds can be either long-lived and stable or outflowing (e.g. [Fabian et al. 2009a](#); [Ishibashi et al. 2018](#)).

Warm absorbers are a common absorption component found in Seyfert 1 galaxies (e.g. [Crenshaw et al. 2003](#)). They consist of partially ionized outflowing clouds located close to the central engine of the AGN. They typically have column densities less than $N_{\text{H}} = 10^{23} \text{ cm s}^{-1}$, are outflowing at $\sim 1000 \text{ km s}^{-1}$ and contain little dust.

A very interesting subclass of AGNs are the Narrow Line Seyfert 1s (NLS1s), which are characterized by the widths of permitted optical lines originating from their BLR. This classification was introduced by [Osterbrock & Pogge \(1985\)](#), and it is based on the width of the broad $\text{H}\beta$ line. Seyfert 1s that have $\text{H}\beta$ widths less than 2000 km s^{-1} are called NLS1; if the $\text{H}\beta$ widths is greater than 2000 km s^{-1} then they are called Broad Line Seyfert 1 (BLS1). NLS1s are thought to be the younger counterparts to BLS1, with lower black hole masses ([Grupe 1996](#); [Mathur 2000](#)). They presumably accrete at high Eddington fractions ([Pounds et al. 1995](#); [Grupe 2004](#); [Komossa 2008](#)), and are typically hosted in spiral galaxies ([Seyfert 1943](#); [Robertis et al. 1998](#); [Varglund et al. 2022](#)). While NLS1s can host radio jets they are generally radio-quiet objects ([Komossa et al. 2006](#); [Foschini et al. 2012](#); [Berton et al. 2015](#); [Järvelä et al. 2022](#)).

The X-ray spectrum of NLS1s is often very variable both in flux and spectral shape on rapid and long-term time scales ([Leighly 1999a,b](#); [Gallo 2018](#)). The rapid variability seen in these objects indicates a physically small emitting region ([Ponti et al. 2012](#); [Fabian et al. 2015](#)). They typically have steep photon indices ([Brandt et al. 1997](#); [Leighly 1999b](#))

indicating cooler and/or more diffuse corona ([Fabian et al. 2015](#)).

NLS1s often show an excess in the soft X-ray band ($< 3 \text{ keV}$) ([Puchnarewicz et al. 1992](#); [Boller et al. 1996](#); [Grupe et al. 1998](#); [Waddell & Gallo 2020](#)), the origin of which is still up for debate. This spectral feature is present in BLS1s but is stronger in NLS1s (e.g. [Waddell & Gallo 2020](#)). It could be the result of partial covering of the central engine (e.g. [Tanaka et al. 2003, 2004](#); [Gierliński & Done 2004](#)), or the result of relativistically blurred soft emission lines from the accretion disc ([Ballantyne et al. 2001](#); [Fabian et al. 2009b](#)). The soft excess may also originate from a secondary warm corona existing on top of the accretion disc (e.g. [Magdziarz et al. 1998](#)). The soft excess may have different mechanisms depending on the source. Typically, it is one of the most variable components of the X-ray spectra of an AGN (e.g. [Boller et al. 1996](#); [Leighly 1999b](#)).

Mrk 1239 may be unlike any other NLS1 studied to date. It presents remarkable challenges and unique features in all energy bands that it has been observed in. Mrk 1239 exhibits bipolar radio jets on both parsec (pc) and kiloparsec (kpc) scales ([Doi et al. 2013](#); [Doi et al. 2015](#)). They appear to be roughly symmetric, subsonic, one approaching and one receding, though which one is which is undetermined. The opening angle also cannot be determined because the location of the radio core is unknown ([Doi et al. 2015](#)).

Mrk 1239 straddles the border between radio-quiete ([Doi et al. 2015](#)) and radio-loud ([Berton et al. 2018](#)) and is classified as a Fanaroff-Riley type I (FRI) radio source ([Fanaroff & Riley 1974](#); [Doi et al. 2015](#)), where radio emission is most intense in the center of the galaxy and decreases intensity with increasing radius. [Buhariwalla et al. \(2023\)](#) overplotted the soft band emission and the radio contours produced by [Järvelä et al. \(2022\)](#) to show that the soft X-ray emission is asymmetric and extended from the center of the galaxy (see Fig 1 of [Buhariwalla et al. 2023](#)).

Mrk 1239 shows an intriguing infrared spectrum, with a blackbody emission feature attributed to hot dust from the torus ([Rodríguez-Ardila & Mazzalay 2006](#)), with a dust temperature of $T = 1210 \text{ K}$. Polycyclic aromatic hydrocarbon (PAH) emission has been detected in the central $\sim 400 \text{ pc}$ of Mrk 1239 indicating an upper limit of star formation of $7.5 \text{ M}_{\odot} \text{ yr}^{-1}$ ([Ruschel-Dutra et al. 2016](#)).

The optical spectra of Mrk 1239 were used in the original definition of NLS1s by [Osterbrock & Pogge \(1985\)](#). The FWHM of the $\text{H}\beta$ has been recently measured to be between 800 km s^{-1} ([Gravity Collaboration et al. 2023](#)) and 1300 km s^{-1} ([Husemann et al. 2022](#)). The extinction of Mrk 1239 is measured to be $E_{B-V} = 1.6$ ([Pan et al. 2021](#); [Feltre et al. 2023](#)). Mrk 1239 is a highly polarized source ([Goodrich 1989](#); [Pan et al. 2019, 2021](#)) whose optical band shows evidence of two distinct regions of polarization. One

of which is thought to be associated with the hot dust seen in the NIR band (Rodríguez-Ardila & Mazzalay 2006).

The X-ray band is where Mrk 1239 is truly unique. The broadband continuum of this object shows an incredibly strong soft excess, a possible broad iron line and a Compton hump (Buhariwalla et al. 2020). The continuum was originally reported to be heavily obscured by a partial covering absorber with a column density in excess of $N_H = 3 \times 10^{23} \text{ cm}^{-2}$ (Grupe et al. 2004).

Excess emission at 0.9 keV was originally reported as the Ne IX triplet (Grupe et al. 2004). Due to the absence of the O VII triplet, the source was inferred to have an overabundance of Ne. Later, this feature was interpreted by Buhariwalla et al. (2020) as collisionally ionized emission (CIE), possibly from a region of star formation in the host galaxy. The star formation rate (SFR) measured using the X-ray spectra was $\simeq 4 - 6 M_\odot \text{ yr}^{-1}$, while the SFR predicted in other bandpasses is $\leq 7.5 M_\odot \text{ yr}^{-1}$ from PAH measurements (Ruschel-Dutra et al. 2016); $3.47 \pm 0.26 M_\odot \text{ yr}^{-1}$ from SED fitting (Gruppioni et al. 2016); and $2.1^{+0.5}_{-0.4} M_\odot \text{ yr}^{-1}$ from IR measurement (Smirnova-Pinchukova et al. 2022).

Buhariwalla et al. (2020) performed a multi-epoch, broadband analysis of all X-ray data available to attempt to understand this galaxy. The soft excess of Mrk 1239 is observed to be remarkably constant over a ~ 20 year period. This was attributed to the physically large scale of the CIE visible because of the heavy absorption of the AGN continuum. The AGN continuum was again interpreted as partial covering; however, blurred reflection was not ruled out. Further data were needed to explore the soft band emission and AGN continuum.

The first high-resolution spectrum of Mrk 1239 was reported by Buhariwalla et al. (2023). Ionized emission lines were detected between 0.4–1.7 keV (7–35 Å); however, due to the dim nature of the source, no continuum was observed. The ionized emission was determined to originate from two distinct plasmas: the CIE and a second photoionized plasma (PIE). The photoionized plasma was found to be ionized by the AGN at a torus-like distance and possibly outflowing at $\sim 660 \text{ km s}^{-1}$. The SFR measured was $\sim 3 M_\odot \text{ yr}^{-1}$, consistent with other measurements. The presumed large scales of the plasma were consistent with the extended and asymmetric X-ray emission seen in the *Chandra* image (Buhariwalla et al. 2023).

This paper presents an X-ray broadband timing and spectral analysis of Mrk 1239 with new data from *XMM-Newton*, *NuSTAR*, and *Swift*. These data were collected primarily in late 2021 and include a joint *XMM-Newton* and *NuSTAR* observation with two *Swift* monitoring campaigns. In Section 2, the new observations and data reduction techniques are summarised. Section 3 examines the timing analysis, including the rapid and long-term variability. Light curves, hardness-

flux diagrams and principal component analysis are explored. In Section 4, the spectra are analyzed, beginning first with the soft band below 2 keV, then the hard band above 4 keV, and finally, the broadband 0.3 – 25 keV spectra are analyzed. A spectral variability analysis is completed in Section 5. The results are discussed in Section 6, and conclusions are drawn in Section 7.

2. OBSERVATIONS AND DATA REDUCTION

Observations of Mrk 1239 began on 2021-11-04 with both *XMM-Newton* (Jansen et al. 2001) and *NuSTAR* (Harrison et al. 2013). The *XMM-Newton* observation concluded on 2021-11-05, while the *NuSTAR* observation concluded on 2021-11-06. Each observatory obtained ~ 100 ks of on-source time. Mrk 1239 entered a flaring state soon after the *XMM-Newton* observation concluded (see Figure 3, and Section 3.3 for details). The data used for spectral analysis is listed in Table 1. A second data set comprising *Swift* (Burrows et al. 2004) snapshots was also obtained and will be present here; the data for these observations is listed in Table 2.

2.1. *XMM-Newton*

The *XMM-Newton* data were processed using the *XMM-Newton* Science Analysis System, SAS V17.0.0. An event list was created from the Observation Data Files (ODF) using EPPROC and EMPROC for the PN and MOS instruments, respectively. Light curves were generated using EVSELECT, and TABGTIGEN was implemented to remove all times when the background had evidence of flaring. No evidence of pileup was found in the PN and MOS data. For both the PN and the MOS spectra, the source data was extracted from a circular region 35'' centred on Mrk 1239, while the background was extracted using a circular region of 50'' on the same chip. Response files were generated using RMFGEN and ARFGEN. We checked whether changes of the PN effective area measured empirically with *NuSTAR*, which were outlined in Technical Note 230¹ (hear after TN230) had a significant impact on our conclusions. This was done by running ARFGEN with the flag APPLYABSFLUXCORR=YES included. We find that including this flag had a minimal effect on PN spectra. There was not a significant impact on our measured parameters or conclusions. Only the PN data were used for spectral modelling, while the MOS data were used for qualitative comparisons and consistency checks.

2.2. *NuSTAR*

The FPMA and FPMB data were extracted from a source region of 75''. A background was selected from the same chip

¹ www.xmmweb.esac.esa.int/docs/documents/CAL-TN-0230-1-3.pdf

(1) Observatory	(2) Observation ID	(3) Instrument Name	(4) Label	(5) Start date (yyyy-mm-dd)	(6) Duration [s]	(7) Exposure [s]	(8) Counts	(9) Energy range
<i>XMM-Newton</i>	0891070101	PN	Low State	2021-11-04	105000	79175	42042	0.3 – 10 keV
<i>NuSTAR</i>	60701038002	FPMA/FPMB		2021-11-04	110050	101641	8841	4 – 30 keV*
		FPMA/FPMB		2021-11-05	106689	99177	17125	4 – 30 keV*
<i>Swift</i>	00031685,00081986	XRT	SwiftAve	-	-	39777	1094	0.3 – 10 keV

Table 1. Observations log for Mrk 1239. The observatory used for analysis is listed in Column (1). The observation ID and instrument name are given in columns (2) and (3), respectively. The label used in this work is given in Column (4). The start date of each observation is given in Column (5). The duration of each observation, total exposure time and total counts for each observation are given in columns (6), (7), and (8), respectively. The energy of each observation used is given in Column (9). The summed duration, exposure and counts are reported for *NuSTAR* FPMA and FPMB. *This is the energy range used for all *NuSTAR* light curves unless otherwise stated. The energy range used for spectral fitting was 4 – 25keV due to loss of signal to noise at higher energies in the uncombined spectra.

with a region of 120". The data were processed with CALDB index version 20210315, using NUPRODUCTS. Good time intervals (GTI) were generated using GTIBUILD and used to extract a low flux (low state) and high flux (high state) spectrum for both FPMA and FPMB (see Section 3.3 for details). The *NuSTAR* data were optimally binned using FTGROUPPHA.

We note a difference in flux between the *NuSTAR* and PN flux between 3–4 keV. We determined it was not due to a tear in the Multi-Layer Insulation (MLI), as the discrepancy was seen in both detectors, not just FPMA (Madsen et al. 2020). We also tested to see if the discrepancy was due to changes in the effective area of PN as per TN230; again, we found this correction insufficient for the data. We note the source is relatively dim at 3 keV, approaching the background level in *NuSTAR*. Thus, ignoring all *NuSTAR* data below 4 keV does not influence the results.

2.3. *Swift*

In the weeks surrounding the deep observations of Mrk 1239, *Swift*-XRT took several snapshot observations of the AGN approximately every two days. In December 2022, ten more snapshot observations were taken. These observations, along with the two archival observations, were compiled for analysis. The details of these observations can be found in Table 2.

The *Swift* XRT spectra were created from the *Swift*-XRT data product generator (Evans et al. 2009)². A spectrum was extracted for each observation ID listed in Table 2. The data were binned into ten bins using GRPPHA. Individual *Swift* spectra can be seen in Appendix A. The light curve binned by observation ID was also extracted using the product generator with two energy bins, 0.3 – 3 keV and 3 – 10 keV.

A final average *Swift* spectrum was also extracted using *Swift*-XRT data product generator. It contains all the data

(1) Observation ID	(2) Start date (yyyy-mm-dd)	(3) Duration [s]	(4) Count Rate [cps]
00031685001	2010-04-13	3616	0.035 ± 0.004
00081986001 [†]	2019-06-17	6216	0.047 ± 0.003
00031685002	2021-10-29	1596	0.047 ± 0.006
00031685003	2021-10-31	1431	0.030 ± 0.005
00031685004	2021-11-02	1573	0.034 ± 0.005
00031685005	2021-11-04	1648	0.054 ± 0.007
00031685006	2021-11-06	1491	0.062 ± 0.008
00031685007	2021-11-08	1618	0.059 ± 0.007
00031685008	2021-11-10	814	0.038 ± 0.008
00031685009	2021-11-12	1683	0.083 ± 0.008
00031685010	2021-11-14	1701	0.039 ± 0.008
00031685011	2022-11-23	1988	0.031 ± 0.005
00031685012	2022-11-26	1532	0.032 ± 0.005
00031685013	2022-11-29	2053	0.031 ± 0.005
00031685015	2022-12-05	2058	0.019 ± 0.004
00031685016	2022-12-08	1965	0.021 ± 0.004
00031685017	2022-12-11	1439	0.034 ± 0.006
00031685018	2022-12-15	1231	0.023 ± 0.006
00031685019	2022-12-18	2151	0.025 ± 0.004
00031685020	2022-12-21	2087	0.050 ± 0.011

Table 2. Observations log for the *Swift* monitoring campaign of Mrk 1239. The *Swift* observation IDs are listed in Column (1). The start date of each observation is given in Column (2), and the duration of each observation and the 0.3 – 10 keV count rates for each observation are given in Columns (3) and (4), respectively. [†]This observation was simultaneous with the 2019 *NuSTAR* observation. The table is divided into three sections: the first contains two historical observations, the second is the *Swift* monitoring surrounding the deep *XMM-Newton*-*NuSTAR* observation, and the third is the second monitoring campaign.

in Table 2, resulting in a total exposure time ~ 40 ks. The spectrum was optimally binned using FTGROUPPHA.

² www.swift.ac.uk/user_objects/

3. TIMING ANALYSIS

Buhariwalla et al. (2020) described the soft band (< 2 keV) of Mrk 1239 with three distinct components; the first was the collisionally ionized component, which was interpreted as originating from a region of star formation in the host galaxy. The second was a photoionized component, interpreted as reflection off a torus-like structure. The final component was a relatively featureless component, interpreted as the AGN continuum leaking through the obscuring clouds. The components and interpretation were largely consistent in the RGS analysis of Buhariwalla et al. (2023). In the RGS spectra, the photo and collisionally ionized components are visible, while the third continuum-like component was not distinguished from the background.

One of the driving characteristics that led to the development of the three-component soft band was the unique variability behaviour of Mrk 1239. This object has shown remarkable consistency in the soft band (below 3 keV) while exhibiting typical levels of AGN variability in the hard band (above 3 keV). These new data demonstrate that behaviour to an extreme, placing more restrictions on the primary absorber that obscures the central engine in Mrk 1239 and the nature of the featureless component. In this section, we probe time scales ranging from years long with the unfolded spectrum (Sec. 3.1) to month-long monitoring with two *Swift* monitoring campaigns (Sec. 3.2); to hours with the PN and *NuSTAR* light curves (Sec. 3.3). This allows us to probe the variability of Mrk 1239 like never before. We will conduct a Principal Component Analysis (PCA) in Section 3.4. Finally, we will conclude what the timing analysis of Mrk 1239 can tell us about this unique source in Section 3.5.

3.1. Long-term Time Scales

We begin on the longest time scales, comparing data spanning 20 years. The unfolded spectra of Mrk 1239 compared to a flat ($\Gamma = 0$) power law are presented in Figure 1. The 2001 MOS, 2019 *NuSTAR*, and an average *Swift* spectrum are included to compare how the general spectral shape has changed in the 20 years of observations.

In the soft band below 3 keV, the PN and average *Swift* spectra appear consistent, and both spectra generally agree with the MOS spectra. There has been very little change in the flux and shape of the spectra over the 20 years of observation. This is consistent with the results of Buhariwalla et al. (2020). Differences appear between 3 and 5 keV, where the more recent data is at a higher flux. This does not appear to be a calibration effect arising from the off-axis MOS observation. It may be a decrease in the column density of the neutral absorber that is covering the primary continuum. This is consistent with the previous spectral fitting results in Buhariwalla et al. (2020).

A flare was captured during the 2021 *NuSTAR* observation (see Section 3.3 for details). To compare the spectral

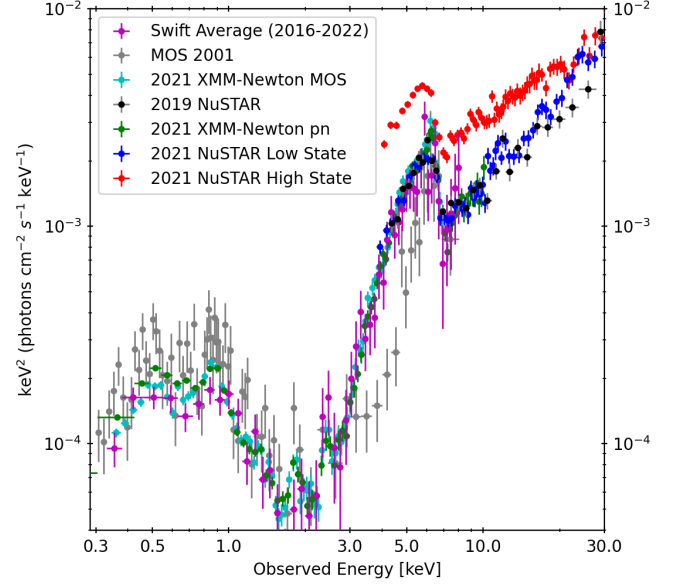


Figure 1. The unfolded spectra of Mrk 1239, showcasing the new pointed 2021 observations with PN (green), *NuSTAR*-low state (blue) and *NuSTAR*-high state (red). For comparison, the average *Swift* spectra (magenta), the 2001 MOS spectra (gray) and 2019 *NuSTAR* (black) are also shown.

variability during the flaring periods, the *NuSTAR* data was divided into a low state and a high state. Figure 3 shows this divide. The low state *NuSTAR* spectrum is simultaneous with the PN spectra and appears nearly identical to the 2019 *NuSTAR* spectrum. The low state spectrum appears slightly brighter above 20 keV. The high state spectrum is brighter than the low state spectra until approximately 20 keV. The rapid variability between 10 – 20 keV indicates continuum changes in the central engine during the flare.

The long-term light curves for this source are presented in Figure 2. Here, we show 20 *Swift* observations spanning 12 years; the spectra for these data can be seen in Appendix A. We also include *Swift*-projected *NuSTAR* and *XMM-Newton* light curves for the 2021 *NuSTAR* and PN data along with the 2001 MOS data. To project the *NuSTAR* light curves into *Swift*-XRT count rates, a conversion factor was estimated using WebPIMMS³, and the average *NuSTAR* spectra fit with an absorbed power law over 4 – 10 keV.

Similarly, the MOS and PN spectra were fitted with an empirical model (BB+PO) to obtain a conversion to the *Swift* count rate using WebPIMMS. The 3 – 10 keV estimated PN count rate was indistinguishable from the *NuSTAR* low state light curve and thus has been left off the figure. The 0.3 – 3 keV light curve and hardness ratio have been included in Figure 2.

³ <https://heasarc.gsfc.nasa.gov/cgi-bin/Tools/w3pimms/w3pimms.pl>

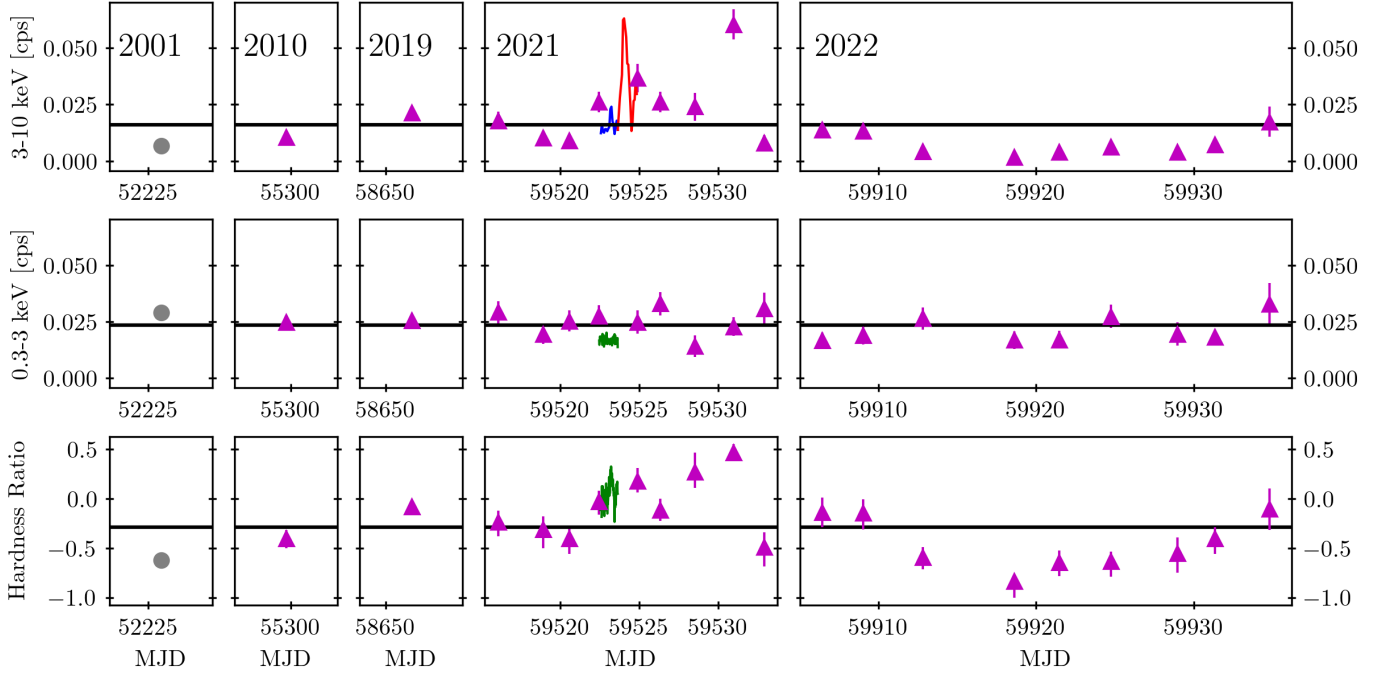


Figure 2. The light curves of Mrk 1239 for the *Swift*-XRT monitoring campaign, with MOS and 2021 *NuSTAR* data projected into *Swift* count rates (see text for details). Each column presents data from a different epoch and the year of the epoch can be found in the top panel. *Top panel:* The hard band (3 – 10 keV) light curve for XRT is shown in magenta, while the 3 – 10 keV light curve for *NuSTAR* is shown in red (high state) and blue (low state). The 2001 MOS data is shown in the first column and is in grey. *Middle panel:* The soft band (0.3 – 3 keV) for XRT is magenta, and the average *Swift* count rate is drawn in black. Notice the remarkable constancy displayed in the soft band. For completeness, the PN 0.3 – 3 keV light curve is also projected into a *Swift* count rate. It is shown in green. *Bottom panel:* The normalized hardness ratio of the XRT light curves, with the soft and hard bands shown in the panels above. The *Swift* average hardness ratio is shown in the black line. For completeness the PN hardness ratio is shown in green, calculated in the same bands that the *Swift* hardness ratio is.

Throughout this work, we use the normalized hardness ratio given by $HR = \frac{H-S}{H+S}$, where H and S are the hard and soft bands, respectively. The exact hard and soft bands used will be clearly stated. The data has sufficient counts in the *XMM-Newton* and *NuSTAR* light curves to be treated as Gaussian. However, the *Swift* snapshots contain limited counts and thus fall into the Poisson regime. For these data, we utilize BEHR⁴ (Park et al. 2006). The value of the hardness ratio is taken from the median, and the uncertainties are at 1σ .

We also use fractional variability (F_{var}) to explore the timing properties of the *Swift* data and utilized the method given by Edelson et al. (2002)⁵ to calculate the error bars (σ_{Fvar}), specifically:

$$F_{var} = \sqrt{\frac{S^2 - \langle \sigma_{err}^2 \rangle}{\langle X \rangle^2}}, \quad \sigma_{Fvar} = \frac{1}{F_{var}} \sqrt{\frac{1}{2N} \frac{S^2}{\langle X \rangle^2}}. \quad (1)$$

⁴ Bayesian Estimation of Hardness Ratios <https://hea-www.harvard.edu/AstroStat/BEHR/>

⁵ See appendix A1 of Edelson et al. (2002) for the derivation of the uncertainty.

Here S^2 represents the variance of the data, $\langle X \rangle$ is the mean count rate, $\langle \sigma_{err}^2 \rangle$ is the mean of the square of the standard error, and N is the number of data points in the light curve.

The long-term *Swift* light curve shows the extreme variability of Mrk 1239 above 3 keV. Between 2001-2022, the hard band exhibits fluctuations around the average hard count rate. While the soft count rate remains relatively consistent. The fractional variability of the *Swift* soft data is $12 \pm 8\%$, while the fractional variability of the hard band is $83 \pm 14\%$. We caution, however, as the Edelson method assumes Gaussian data and the *Swift* hard band is in the Poisson regime. Despite this, there appears to be a stark contrast between the variability in amplitude in each band, indicating a disconnect between the hard and soft emitting regions.

Comparing the *Swift* soft band to its average value results in $\chi^2/\text{dof} = 28/19$ ($p = 0.08$, where p is the probability of the null hypothesis that the light curve is constant in time). In contrast, compared to their mean values, the hard band and the hardness ratio highlight significant variability, resulting in a fit statistic of $\chi^2/\text{dof} = 353/19$ ($p < 0.0001$) and $\chi^2/\text{dof} = 152/19$ ($p < 0.0001$), respectively. While we can neither accept nor reject the null hypothesis that the data is constant in time for the soft band, we can reject the null for

the hard band and the hardness ratio. It appears there is a total disconnect between the soft and hard bands in Mrk 1239.

3.2. Intermediate Time Scales

Looking at each of the approximately month-long *Swift* light curves in isolation, we can begin to probe the variability of this source on intermediate timescales. During the 2021 monitoring campaign, there are rapid changes in the hard flux, suggesting some flaring activity. One of these flaring events occurred during the *NuSTAR* observation. Another occurred several days later on November 12th (MJD 59530), suggesting that Mrk 1239 was undergoing multiple flaring events during this epoch. The *Swift* soft band shows no evidence of change in the count rate during or after this observation.

In 2022, the hard count rate drops to as low as 10% the average count rate. These low-flux events appear with a drastic softening of the spectra. It is similar to the count rate and hardness ratio observed in Mrk 1239 during the 2001 *XMM-Newton* observation, while the source was obscured with a higher column density neutral absorber. A second average *Swift* spectrum was created using the softest *Swift* observations from 2022. The spectrum is comparable to the 2001 MOS spectrum above 3 keV, suggesting that the source was in a similar state at the time of these observations. All other observations of Mrk 1239 since 2019 have shown a less absorbed hard continuum compared to 2021. Examining the general shape of the 2022 hardness ratio where the data starts near the average, then drops to the lowest hardness ratio observed by *Swift* before returning to the average almost a month later, a possible explanation could be a transiting obscuration event such as the one seen in NGC 6814 (Gallo et al. 2021) but on much longer time scales. More data would be required to confirm such transient events.

Based on the *Swift* monitoring and data above 3 keV, the continuum of Mrk 1239 undergoes periods of rapid flux changes and intense dimming. The nature of the continuum variability will be investigated below.

3.3. Rapid Time Scales

Figure 3 shows the 0.3 – 10 keV PN light curve and the 4 – 30 keV *NuSTAR* light curve binned to 1000 s and by orbit (5780 s), respectively. In the second half of the *NuSTAR* observation, the 4 – 30 keV count rate jumped from ≈ 0.2 to nearly 1 cps in approximately 30 ks.

Although *XMM-Newton* was not pointed at the source during the *NuSTAR* flare, a smaller brightening event was captured by both telescopes at around 60 ks into the *XMM-Newton* observation. Figure 4 shows the PN light curve in five energy bands: 0.3–1 keV, 1–3 keV, 3–4 keV, 4–6 keV, and 6–10 keV, all binned to 2000 s, as well as the *NuSTAR* low state light curves in the 4–6 keV, 6–10 keV, and 10–30 keV band.

The variability, particularly between 60 – 85 ks, is constrained to the bands between 3 – 30 keV. Below 3 keV, there is no evidence of any variability. The soft light curves here remain constant for the duration of the observation. The PN 0.3 – 1 keV and 1 – 3 keV bands have $\chi^2/\text{dof} = 95/91$ ($p = 0.37$) and $72/91$ ($p = 0.93$), respectively, when compared with their mean.

When compared to a constant, the 3–4 keV, 4–6 keV, and 6–10 keV light curves resulted in a $\chi^2/\text{dof} = 202/91$ ($p < 0.0001$), $344/91$ ($p < 0.0001$) and $157/91$ ($p < 0.0001$), respectively. Similarly, the *NuSTAR* light curves are also inconsistent with constants with $\chi^2/\text{dof} = 86/18$ ($p < 0.0001$), $97/18$ ($p < 0.0001$) and $82/18$ ($p < 0.0001$) for the 4–6 keV, 6–10 keV, and 10–30 keV bands, respectively. Thus, we reject the null hypothesis that the light curves are constant in all energy bands above 3 keV with more than 99.99% confidence. This further indicated that changes to the continuum flux do not propagate to the low energy band on short-time scales.

Hardness-flux plots were constructed for *Swift*, *XMM-Newton* and *NuSTAR* data to further demonstrate this disconnect. The left panel of Figure 5 shows the hardness-flux plot for the PN and *Swift* data with a soft band of 0.3 – 3 keV and a hard band of 3 – 10 keV. The *Swift* data have the same time binning as outlined in Table 2, and PN data are again in 1000 s bins. The average flux was estimated using the average spectra of each data set; this was used to convert cps to flux. The data shows a clear harder when a brighter trend on short (PN) and long (*Swift*) time scales. We use Spearman’s rank correlation coefficient (r_s) to evaluate correlations between the hardness ratio and flux. The r_s and the associated p-value⁶ are calculated using SCIPY⁷ (Virtanen et al. 2020). Similar to the Pearson correlation coefficient, positive values of r_s indicate a positive correlation, and negative values of r_s indicate a negative correlation.

The 0.3 – 10 keV *Swift* and PN light curves show strong positive correlations, with $r_s = 0.77$ and $r_s = 0.61$, respectively ($p < 0.00007$ for both). This indicates that the source becomes harder as the flux increases. The flux range for *Swift* is much larger than for PN; we might expect the PN data to continue to follow the *Swift* trend with a more variable observation. This harder-when-brighter trend in the 0.3 – 10 keV is not seen in most NLS1 but has been reported in Mrk 1239 (Buhariwalla et al. 2020). This points to AGN contribution below 3 keV being absent from detection in Mrk 1239.

Above 3 keV, a hardness-flux plot was constructed for the PN data with a hard band of 5 – 10 keV and a soft band of 3 – 5 keV. Here, $r_s = -0.35$ ($p < 0.0006$) for the

⁶ From here the null hypothesis is that there is no correlation between the variables

⁷ <https://docs.scipy.org/>

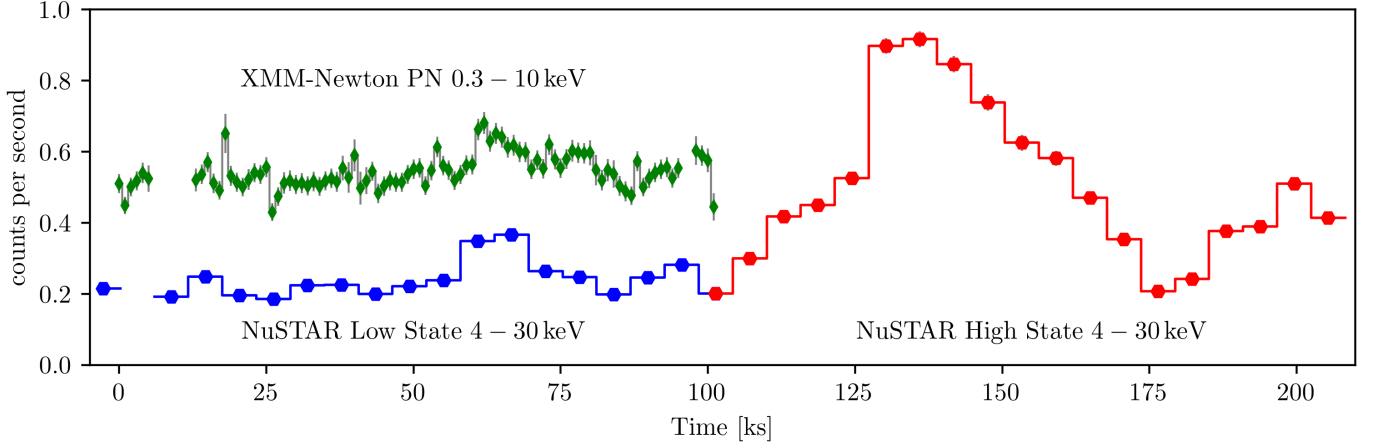


Figure 3. Light curves from the deep *XMM-Newton* and *NuSTAR* observations. A flaring event was detected during the later half of the *NuSTAR* observation. The data were divided into low and high states. This divide illustrates the times when the *NuSTAR* spectra are extracted in low and high states. The PN data are in green diamonds, while the NuLow and NuHigh data are in blue and red hexagons, respectively. For all *NuSTAR* data presented, FPMA and FPMB are summed. Zero seconds marks the start of the PN exposure.

un-binned data, which indicates a moderate negative correlation between the flux and the hardness ratio. To further explore this connection, we bin the data into five flux bins. The Spearman’s rank correlation coefficient then becomes $r_s > -0.999$, indicating a strong negative correlation ($p < 0.00005$).

The right panel of Figure 5 shows a hardness-flux plot for the *NuSTAR* observation. Here, $r_s = -0.67$, ($p < 0.00001$) indicating a strong negative correlation. Above 4 keV, Mrk 1239 exhibits the expected softer when brighter behaviour.

3.4. Principal Component Analysis

Principal Component Analysis (PCA) is a mathematical method to reduce the dimensionality of a multivariate data set. This method deconstructs a set of vectors into a mean vector plus a linear combination of eigenvectors called principal components. After performing PCA, one may reconstruct any input vector by the sum of the mean vector and the principal components scaled to specific values. Each successive principal component will account for less variance than the previous principal component (Ivezić et al. 2019). The amount of variance captured by each principal component is represented by the eigenvalue; this value can be normalized and presented as a percent variance for each principal component (Parker et al. 2013).

We utilize time-resolved spectra as our input vectors, allowing us to probe changes in the spectra. This technique has been used for NLS1 galaxies previously (e.g. Parker et al. 2013; Parker et al. 2014; Gallo et al. 2015), and allows us to see the shape of the variable components between spectra.

We perform a principal component analysis on the various data sets presented in the timing analysis. We probe long-term trends with the 20 separate *Swift* spectra; the *NuS-*

TAR data were divided into orbit-by-orbit spectra for both the 2019 and 2021 observations. Finally, the PN data were divided into 20 spectra of approximately 5 ks exposure time to probe short-term trends.

Using these un-binned spectra, we utilized the PCA code distributed by Parker et al. (2013)⁸. We perform the principal component analysis and extract the first principal component and the first eigenvalue. The principal components can be seen in Figure 6. We see that the *NuSTAR* data suggests a normalization change to explain the variability seen in the observation. Turning towards the PN and *Swift* principal components. We see the same behaviour as previously reported— a lack of variability in the soft band and a change in normalization in the hard band. This trend holds on all time scales from the rapid PN to the long-term (*Swift*) data. The simulated PCA is described in Section 3.5.

3.5. Timing Evidence Supporting 100% Covering Fraction of the AGN Below 3 keV

Buhariwalla et al. (2020) presented a continuum model for Mrk 1239 that required partial covering of the central source. This resulted in emission from the soft band originating from three distinct physical regions: a collisionally ionized component from a star formation region, a photoionized component attributed to distant reflection from the torus, and the partially covered continuum component “leaking through” the partially covering absorber. Analysis of the RGS spectra confirmed the presence of the two emission line components, with the detection of lines from collisionally ionized and photoionized emission lines (see Buhariwalla et al. 2023, for details).

⁸ We port the code from python2 to python3

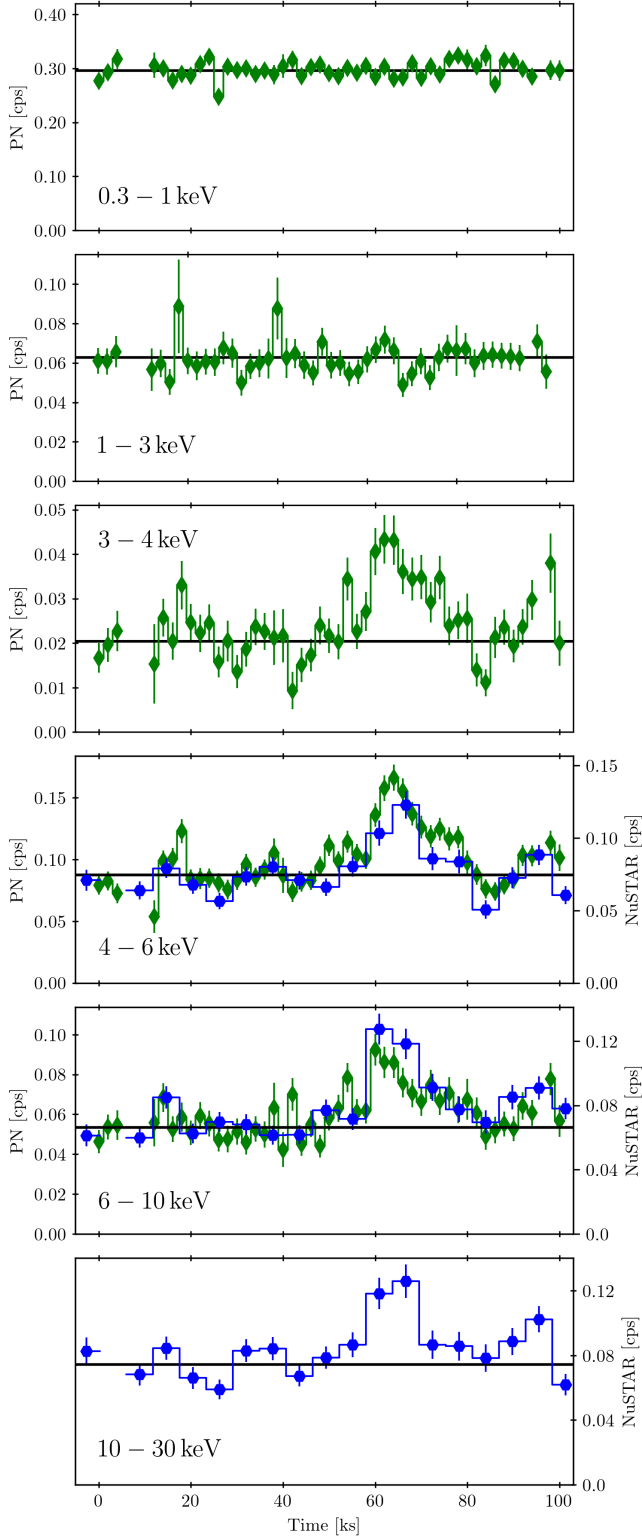


Figure 4. Low state light curves for the PN (green diamonds; left axis) and *NuSTAR* (blue hexagons; right axis) data. The PN light curves are binned to 2000 s and divided into five energy bins. The *NuSTAR* light curves are binned into orbital bins (5780 s) and divided into three energy bins. The energy bins are listed in the panel. Where the instruments overlap in energy, both light curves are shown. The black line shows the average counts per second [cps] in each energy bin.

Utilizing the 2020 best-fit reflection model (see Section 4.2), using a neutral partial cover with $N_{\text{H}} = 25 \times 10^{22} \text{ cm}^{-2}$, $CF = 98\%$, we simulate spectral data with variable strengths of the AGN continuum. The continuum strength was varied such that the $0.3 - 10 \text{ keV}$ count rate ranged between $\sim 0.4 - 0.7 \text{ count s}^{-1}$, consistent with the variation seen in the PN light curves. PCA was performed, and Figure 6 shows the first principal component in black. We see a significant amount of variability below $\sim 2 \text{ keV}$. This is inconsistent with the PN and *Swift* principal components.

The origin of the variability detected in the first principal component is primarily due to the AGN continuum leaking through the partial covering absorber. This is visualized in Figure 7. Here, the best-fit model from 2020 was applied to the 2021 low-state data. We note that the fit to the 2021 data is acceptable and would be considered one of the best-fit models for the low state. The covering fraction was $CF = 98.2^{+0.2}_{-0.4} \%$, and the column density was $N_{\text{H}} = 25^{+2}_{-1} \times 10^{22} \text{ cm}^{-2}$. The high-state data was then included, and the AGN continuum components were allowed to scale to match the flux of the high-state spectra. All other parameters (column densities, covering fractions, photon index, etc.) were linked. This is a drastic example of the flux variations seen in the hard band of Mrk 1239 and is not representative of the flux variation we see in the PN light curve. However, it serves as a visualization of what the hard band of Mrk 1239 is capable of and how that might affect the soft band of this galaxy.

We further explored the effects of the neutral partial covering material to see if any partial covering absorber could be used to reproduce the first principal component of the PN and *Swift* spectra. We simulated sixteen different absorbers with $N_{\text{H}} = 22, 25, 30, 35 \times 10^{22} \text{ cm}^{-2}$, and $CF = 95, 98, 99, 99.5\%$. For each absorbing scenario, we simulated the spectra such that the $4 - 10 \text{ keV}$ count rate ranged between $\sim 0.1 - 0.2 \text{ count s}^{-1}$. This ensured we recovered the variability we saw in the hard band of the PN data. Appendix B shows the first principal component for these simulated data.

None of these absorbers could reproduce the observed first principal component. The results of the PCA simulations indicated that the covering fraction had a stronger influence on the observed variability in the soft band than the column density. However, all absorbers tested showed soft band variation similar to that shown in Figure 6. Thus, even at covering fractions upwards of 99%, the continuum leaking through produces significant flux changes in the soft band of Mrk 1239.

The 2020 best-fit reflection model predicts the $0.3 - 3 \text{ keV}$ observed flux would be $5.4 \times 10^{-13} \text{ erg cm}^{-2} \text{ s}^{-1}$ in the low state, and 1.3×10^{-12} in the high state. This would result in

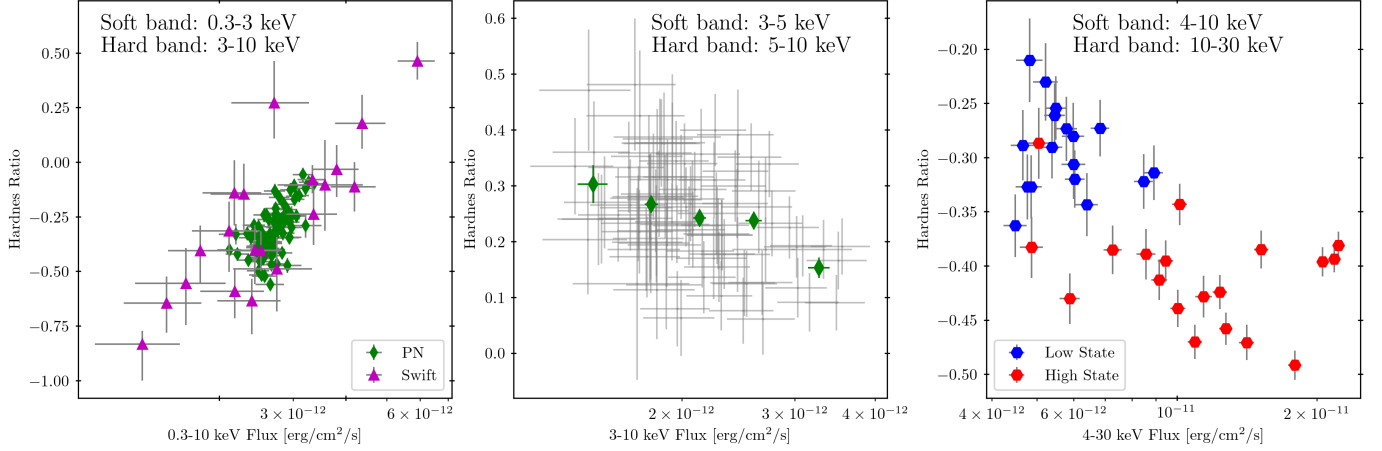


Figure 5. Hardness-Flux plots for the PN *Swift* and *NuSTAR* data. *Left panel:* *Swift* (magenta triangles) and PN (green diamonds) data Hardness-Flux plot. The hard band is taken to be 3 – 10 keV, and the soft band is 0.3 – 3 keV. We see a clear, harder-when-brighter trend in the pointed PN observation and the *Swift* monitoring campaign. *Middle panel:* Hardness-Flux plot for PN data, here the hard band is 5 – 10 keV, and the soft band is 3 – 5 keV. The gray data is un-binned, while the green diamonds show the data binned by flux. *Right panel:* Hardness flux plot for the low state (blue hexagons) and high state (red hexagons) data. The hardness ratio used a hard band of 10-30 keV and a soft band of 4-10 keV. Here, we see the expected soft when brighter behaviour. For all *NuSTAR* data presented, FPMA and FPMB are summed.

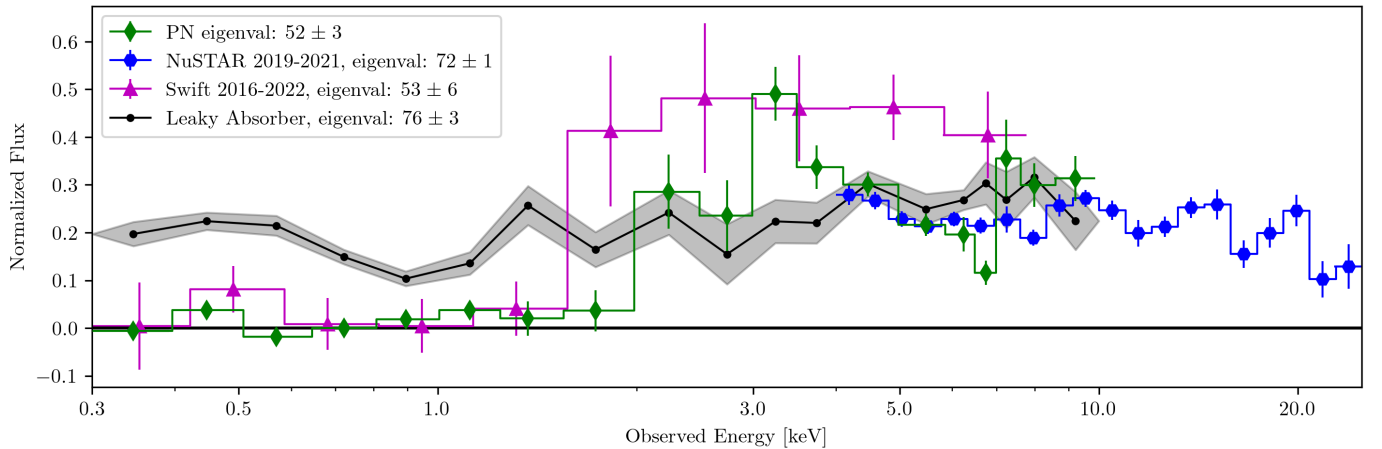


Figure 6. The first principal component for the *Swift* (magenta triangles), PN (green diamonds) and *NuSTAR* (blue hexagons) as well as the simulated leaky absorber based on Buhariwalla et al. (2020) in black. The shaded regions on the simulated data show the uncertainties.

an observed change in flux of a factor of ≈ 2.4 . Nowhere in more than 20 years of observations does the flux of the soft band even approach changing that much. The long-term *Swift* light curves show no evidence of Mrk 1239 exhibiting any soft variability at this level, and the PN light curve showed no evidence of any variability below 3 keV.

The hardness-flux plot for the *Swift* and PN data showed a clear linear, harder-when-brighter trend (Figure 5). All the simulated spectra of Mrk 1239, even with absorbers with parameters at least 5σ greater than those required by the low state data ($CF = 99.5\%$, $N_H = 35 \times 10^{22}$), fail to reproduce the observed first principal component of the PN spectra. This suggests that the soft band of Mrk 1239 is not partially obscured, but completely absorbed by a $N_H \geq 10^{23} \text{ cm s}^{-1}$ cloud. This results in no direct AGN emission below 3 keV.

Instead, the soft band comprises of a physically large region that are not intrinsic to the AGN.

This interpretation would explain why the soft band remains constant in the *Swift* 2022 data while the hard band flux dropped significantly. If the continuum was responsible for a significant amount of flux below 3 keV, then when the hard band dims, so too should the soft.

4. TIME RESOLVED SPECTRAL MODELLING

All spectral data were optimally binned (Kaastra & Bleeker 2016) and background modelled in XSPEC (Arnaud 1996). We used C-statistics (Cash 1979) to evaluate the fit quality throughout. The data were divided into two epochs, the low-state ($t < 100 \text{ ks}$) and the high-state ($t > 100 \text{ ks}$), as seen in Figure 3. The low-state includes PN and *NuSTAR*

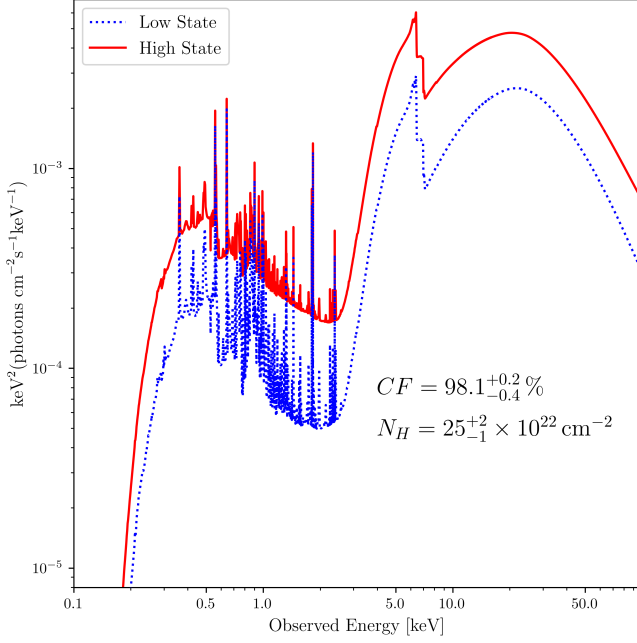


Figure 7. Low state (blue solid line) and High state (red dotted line) best fit partial covering model based on the 2020 best-fit model. The covering fraction of the neutral absorber for both models was $CF = 98.2^{+0.2}_{-0.4} \%$, and the column density was $N_H = 25^{+2}_{-1} \times 10^{22} \text{ cm}^{-2}$ resulting in $\approx 2\%$ of the

continuum leaking through the absorber.

data, while the high-state includes only *NuSTAR* data. Slowly changing or constant parameters (e.g. inclination, column density, ionization) were linked across both epochs. Furthermore, model components whose emission appeared primarily in the soft band (such as photoionized and collisionally ionized plasmas, etc.) were also linked between epochs. A cross-calibration constant was applied to the FPMA and FPMB detector in *NuSTAR* when applicable. The constant was free for FPMB and monitored to ensure it remained within acceptable ranges, as prescribed by *NuSTAR* FAQ⁹ and the calibration work done by Madsen et al. (2015). A Galactic column density of $N_H = 4.43 \times 10^{20}$ (Willingale et al. 2013) was applied to all models and frozen throughout the spectral fitting. Solar abundance in Wilms et al. (2000) were used throughout the spectral fitting.

For model comparison, the corrected Akaike information criterion (AICc) was used (Akaike 1974; Sugiura 1978; Liddle 2007). AIC is defined as $AIC = 2k - 2\ln(\mathcal{L})$ where k is the number of fitted parameters and \mathcal{L} is the maximum likelihood estimator (MLE). The exponential of the C-statistic (C-stat) is related to the MLE ($\mathcal{L} \propto e^{-C\text{-stat}/2}$), thus $C\text{-stat} = -2\ln(\mathcal{L})$ (Tan & Biswas 2012). With the addition

⁹ https://heasarc.gsfc.nasa.gov/docs/nustar/nustar_faq.html

(1)	(2)	(3)	(4)
Model No.	Components	C-stat/dof	AICc
1a	APEC + XSTAR	1390/41	1400
1b	ZPCFABS*APEC + XSTAR	945/39	961.8
2a	APEC + XILLVER	581/40	594.4
2b	ZPCFABS*APEC + XILLVER	581/38	601.5
3a	APEC + XSTAR + XILLVER	213/38	233.6
3b	ZPCFABS*APEC + XSTAR + XILLVER	212/36	242.0
4a	APEC + APEC + XILLVER	201/38	222.4
4b	ZPCFABS*APEC + APEC + XILLVER	182/36	212.0
5a	APEC + ZBB + XILLVER	273/38	293.6
5b	ZPCFABS*APEC + ZBB + XILLVER	50/36	80.4
6a	APEC + ZBREM + XILLVER	154/38	174.3
6b	ZPCFABS*APEC + ZBREM + XILLVER	46/36	75.8
7	ZPCFABS*APEC + ZBREM + XSTAR	63/37	88.4
8a	ZPCFABS*(APEC + ZBREM) + XILLVER	44/36	74.4
8b	ZTBABS*APEC + ZBREM + XILLVER	46/37	71.2

Table 3. Models tested with the PN data $< 2 \text{ keV}$ that do not contain AGN continuum. Column (1) states the model name, Column (2) shows the components as they would appear in XSPEC, Columns (3) and (4) show the C-stat/dof and AICc value for each fit, respectively. The ratios of a selection of these fits can be seen in Figure 8.

of the small sample size correction, we will use:

$$AICc = 2k + C\text{-stat} + \frac{2k^2 + 2k}{n - k - 1}, \quad (2)$$

where n is the number of data points fitted. The second term goes to zero as n becomes large. Thus, AICc is always valid (Sugiura 1978). The difference between the AICc from two models, A and B, $\Delta AIC_{A-B} = AICc_B - AICc_A$, will be used to compare models. We adopt the values of $\Delta AIC \geq 6$ to indicate a significantly better fit. This corresponds to a 95 percent confidence that one model is preferred over the other (Tan & Biswas 2012).

4.1. The Low Energy Spectrum Below 2 keV

We begin with the PN spectra below 2 keV. As the timing analysis demonstrates, the lack of variability in Mrk 1239 requires completely removing the varying AGN continuum from the soft band. Thus, we fit the soft band below 2 keV without any AGN continuum. We list each model tested and their fit statistics in Table 3. Figure 8 showcases the data below 2 keV and a selection of the ratio plots from the models tested.

We begin with the two-component model from the RGS analysis of Buhariwalla et al. (2023), which utilized APEC (Smith et al. 2001) for the collisionally ionized component and a generated XSTAR grid (Kallman & Bautista 2001) for the photoionized component. The grid was based on those used previously for this source (see Buhariwalla et al. 2023) with density fixed at 10^{10} cm^{-3} , and column density logarithmically sampled at ten points between 10^{20} cm^{-2} and 10^{24} cm^{-2} .

The log ionization was sampled linearly at 10 points between $\log \xi = 1$ and 4 [erg cm s^{-1}]. The final grid was

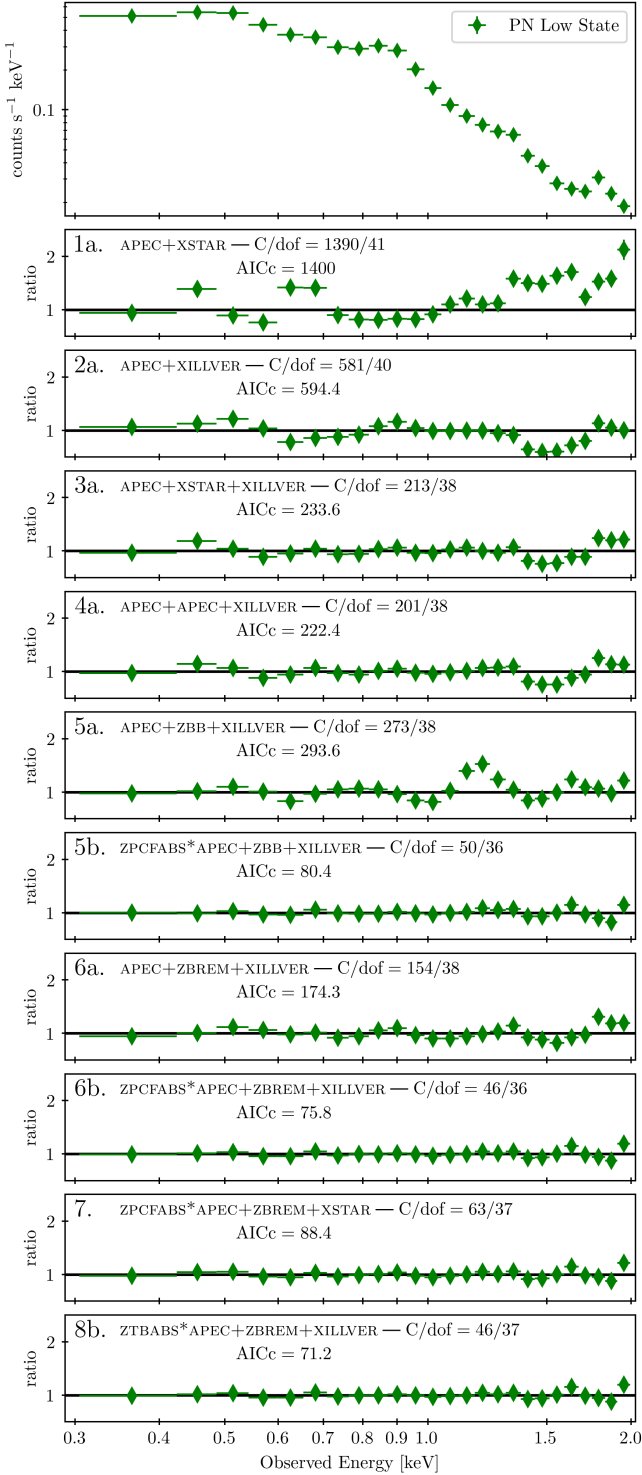


Figure 8. *Top panel:* The 0.3 – 2 keV low state PN data. *Lower panels:* Ratio plots from test models for the PN spectra below 2 keV. The spectral models increase in complexity from top to bottom. Each model is stated in the panel with its ratio plot along with the C-stat/dof and AICc fit statistics. For comparison, all panels share the same energy and ratio axis. The best-fit model can be seen in panel 8b

calculated at 100 steps, with the energy spanning from 0.1 to 50 keV (Buhariwalla et al. 2023). For the APEC component, plasma temperature and normalization were free to vary, while abundance was fixed to solar values.

This initial model produced a fit statistic of $C - \text{stat}/\text{dof} = 1390/41$. The ratio of this fit can be seen in panel 1a of Figure 8. This two-component model was expected to fit the PN data poorly as it contains only the emission components visible from the RGS spectra. It is included here to compare with other photoionized components.

Next, we test a distant reflection component in XILLVER (García & Kallman 2010; García et al. 2013) for the photoionized component. This model takes an input power law continuum and returns a reflected spectrum based on the viewing angle and physical properties of the material from which the photons are reflected. The parameters include a photon index (Γ), high energy cutoff (E_{cut}), iron abundance (A_{Fe}), ionization ($\log \xi$), inclination (i) and normalization. Typically, the photon index is linked to the photon index of the primary continuum (power law). There is no evidence of a power law below 2 keV; thus, Γ was fixed to $\Gamma = 2.5$, a typical value of the photon index found in Mrk 1239 (Buhariwalla et al. 2020; Jiang et al. 2021). The iron abundance was fixed to solar abundance. The ionization, inclination and normalization were free to vary when XILLVER was implemented. This produced a fit of $C - \text{stat}/\text{dof} = 581/40$. The ratio of this fit can be seen in panel 2a of Figure 8. The ionization parameter was similar to the value obtained through the RGS fitting. This produced a significantly better fit than the XSTAR model, with the $\Delta\text{AIC} = 806$ indicating that XILLVER is strongly preferred in the two-component scenario. This behaviour is opposite to what we see in the RGS data. We believe that this difference is due to the densities of the photoionized plasma modelled by XSTAR ($n = 10^{10} \text{ cm}^{-3}$) and XILLVER ($n = 10^{15} \text{ cm}^{-3}$). This is explored further in Section 6.1.1.

Next, we test three component models. The first two components will be APEC + XILLVER, and the third will be either a second ionized emission line component (XSTAR, or APEC) or a smooth continuum-like component such as a black-body (ZBB) or bremsstrahlung (ZBREM, Karzas & Latter 1961; Kellogg et al. 1975). The XSTAR component will have the same parameters free as above while the APEC, ZBB and ZBREM will have their plasma temperature (kT) and normalization free to vary. The ratios for these three models can be seen in Figure 8 (panels 3a, 4a, 5a, and 6a for XSTAR, APEC, ZBB and ZBREM respectively). Each model produced a superior AICc than the two-component model, with the data favouring model 6a (APEC + ZBREM + XILLVER). The ΔAIC compared to 6a are as follows: $\Delta\text{AIC}_{6-3} = 59.3$ compared to model 3a (APEC + XSTAR + XILLVER); $\Delta\text{AIC}_{6-4} = 48.1$ compared to model 4a (APEC

+ APEC + XILLVER); and $\Delta\text{AIC}_{6-5} = 119.3$ compared to model 5a (APEC + ZBB + XILLVER). The bremsstrahlung component appears to be the most favoured third component.

Models 1 to 6 have corresponding second part (i.e. part b), in which the APEC component is absorbed with a neutral partial cover (ZPCFABS). Corresponding models 1, 4, 5 and 6 improve by including the partial cover. The $\Delta\text{AIC}_{a-b} = 438.2, 10.4, 213.2$ and 98.5 for models 1, 4, 5, and 6, respectively. Models 2 and 3 are worse with the inclusion of the neutral partial cover and are only included in Table 3 for completeness.

For the third component of the soft band model, we find that a smooth continuum component is favoured over a third emission line component. Models 3a and 4b are the best fit three emission line models. However, the $\Delta\text{AIC} > 100$, favouring models 5b and 6b, which contain a smooth continuum-like component (ZBB and ZBREM, respectively).

The best model for the PN data below 2 keV requires a smooth continuum-like spectrum in addition to the plasma emission lines. However, the lack of variability < 2 keV indicates the third component can not be the AGN continuum. Here, the shape of the smooth continuum-like component is either blackbody or bremsstrahlung with a preference for the latter ($\Delta\text{AIC}_{5-6} = 4.6$). Table 4 reports the best-fit values for several parameters here, we note that the error for these parameters was determined using the default XSPEC error command. The temperature of the bremsstrahlung emission is $kT = 0.25 \pm 0.03$ keV, while the temperature of the blackbody was $kT = 0.098 \pm 0.005$ keV. The parameters for the neutral partial cover and APEC components are comparable in all models. Even with the addition of the partial cover on the APEC component, the temperature of the collisionally ionized plasma is comparable with that measured from the RGS spectra (Buhariwalla et al. 2023). The temperature of the ZBREM component is very low, and we would not expect a physical plasma like this to exist. At low plasma temperatures (< 100 eV), we would expect the two-photon continuum and recombination continuum to dominate over the bremsstrahlung continuum (Böhringer & Werner 2010). Thus, we are using the ZBREM and ZBB components to characterize the shape of the spectra and their relative strength.

We include model 7, ZPCFABS*APEC + ZBREM + XSTAR for completeness. This is the model that we would expect to work best on the RGS data, as the RGS data strongly prefers XSTAR over XILLVER. We can see in Figure 8 that the data are well fit except around 0.5 keV, which is the location of the O VII triplet. This will be discussed in Section 6.1.1.

Finally, we tested the effect of absorption on all three components in model 6. These have been reported in Table 3 as models 8a and 8b. First, we find that the photoionized emission cannot be absorbed. In all absorption tests, the data prefer the photoionized component to be unabsorbed.

(1) Components	(2) Parameter	(3) 5b	(4) 6b	(5) 8b
ZPCFABS	$N_H [10^{22}/\text{cm}^2]$	$0.74^{+0.14}_{-0.05}$	$0.77^{+0.05}_{-0.24}$	
	$CF [\%]$	> 95	> 92	
ZTBABS	$N_H [10^{22}/\text{cm}^2]$			$0.73^{+0.06}_{-0.05}$
APEC	$kT [\text{keV}]$	0.79 ± 0.03	$0.80^{+0.04}_{-0.03}$	0.80 ± 0.03
ZBB	$kT [\text{keV}]$	0.098 ± 0.005		
ZBREM	$kT [\text{keV}]$		0.23 ± 0.02	$0.23^{+0.02}_{-0.03}$

Table 4. Best-fit parameters for the ZPCFABS (or ZTBABS), APEC, and ZBREM (or ZBB) components in models 5b, 6b and 8b. Column (1) states the model component, Column (2) states the parameter, and Columns (3), (4) and (5) show the best-fit value for models 5b, 6b, and 8b respectively.

The fit was significantly worse when all three emission components were fit with the same partial covering component. When all three components have separated absorption, the N_H and covering a fraction of the absorber applied to the photoionized component becomes very small. Next, we find a small fit improvement by absorbing the ZBREM and APEC components with the same partial covering component, $\Delta\text{AIC}_{6b-8a} = 1.4$. This is not at the threshold to be considered statistically significant; thus, we considered these models equivalent. Finally, we test the absorber ZTBABS, to represent a completely absorbed scenario. We find that under these conditions, the APEC component can be absorbed, but the ZBREM component cannot. The C-stat between 6b and 8b is the same; however, ZTBABS requires one fewer free parameter than ZPCFABS; thus, the AICc value is smaller. We do not show model 8a in Figure 8, as the ratio plot produced is virtually identical to models 6b and 8b.

Model 8b produces the smallest AICc value and will be the model we use moving forward. However, we cannot exclude models 6b and 8a at the 95 percent confidence level. We will revisit the scenarios that produced all three models when we consider the physical interpretation of these results in Section 6.1.

To explore the validity of these results, we first tested to see if removing all *XMM-Newton* data below 0.5 keV would eliminate the need for a smooth continuum component. This was done to check if possible calibration uncertainties led to the continuum requirements. The smooth continuum component is most present at the softest energies; thus, there was concern that its presence was a statistical artifact. We find that the data still favour the inclusion of the smooth continuum with $\Delta\text{AIC} = 35.5$, even when all data below 0.5 keV is ignored. Next, we tested if the component was also necessary with the MOS instruments. We find that the inclusion of a smooth continuum component is necessary ($\Delta\text{AIC}_{6b-2b} > 450$) for the combined MOS spectra.

Next, we explored how the best-fit model fits the RGS data. We applied model 7 to the data outlined in Buhariwalla et al. 2023. We find that the smooth continuum component is not necessary in the RGS spectra. However, we believe this is

due to the dim nature of the source. This will be discussed further in Section 6.1.3. Without the need for a smooth continuum, we turn to models 1a and 1b. When they are applied to the RGS data, the $\Delta\text{AIC}_{a-b} = 19.9$. Thus, we can state that including partial covering of the APEC component is statistically significant when fitting data from all *XMM-Newton* detectors. The discrepancy between the PN data favouring XILLVER and RGS data favouring XSTAR will be discussed in Section 6.1.1.

4.2. The High Energy Spectrum Above 4 keV

Now, we turn our attention to the spectra above 4 keV. Here, the AGN component of Mrk 1239 can shine through the heavy obscuration that occludes the soft emission. This is also where the *NuSTAR* flare becomes prevalent. All models employ a neutral absorber (ZTBABS) with a column density of at least $N_{\text{H}} = 10^{23} \text{ cm}^{-2}$ to ensure that the soft band is completely absorbed. We test several models to account for the AGN emission. Figure 9 shows the data and ratios of a sample of these fits. All parameters are linked between the PN and *NuSTAR* data for all fits. Cross-calibration constants were free to vary between the FPMA and FPMB instruments. Despite the known calibration issues between *XMM-Newton* and *NuSTAR* above 6 keV (see TN230 for details), we keep the response the same and link Γ between *NuSTAR* and PN data. This is because inadequacies in the models, especially in the early testing phase, far outweigh cross-calibration issues with the data.

The ratio of an absorbed power law fit can be seen in panel A of Figure 9. This does not describe the broad feature between 6 and 7 keV. There may also be an emission line feature around 6.4 keV. Furthermore, there is an excess of emission above 10 keV that appears to peak at ~ 20 keV, possibly suggesting the presence of a Compton hump.

Next, we explored the preferred continuum scenario from Buhariwalla et al. (2020), Ionized Partial Covering (IPC), which can be seen in panel B of Figure 9. In this scenario, the curvature seen in the spectra is a result of absorbing material partially obscuring the central engine, blocking some fraction of the emission while letting the rest pass through the material (see Holt et al. 1980; Tanaka et al. 2004; Buhariwalla et al. 2020).

The original model used for Mrk 1239 was XILLVER + ZX-IPCF*ZPCFABS*PO. We have shown that the absorption of the soft band is complete; thus, the neutral partial cover (ZPCFABS) is replaced with neutral absorption (ZTBABS). The XILLVER component is included to model the neutral Fe K α line at 6.4 keV. This was an improvement over the absorbed power law. However, the curvature of the spectrum was not easily reproduced with absorption. The model over-predicts the emission at ~ 6.7 keV. We then attempted to fit the data with as many absorbing (ionized and neutral) components as

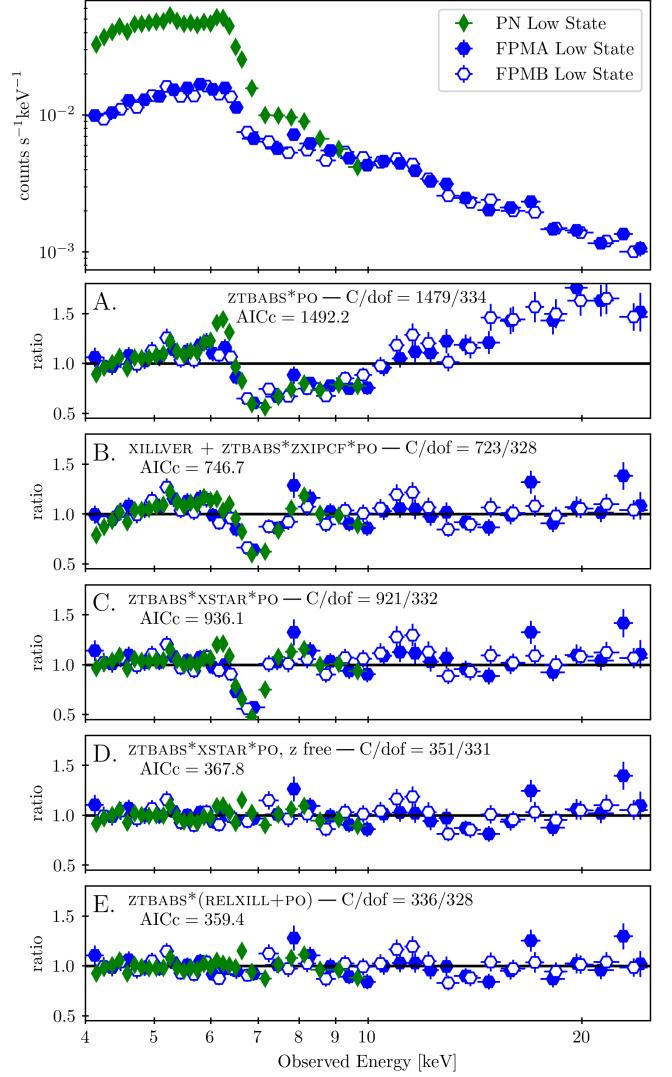


Figure 9. *Top panel:* The PN data between 4–10 keV, and the *NuSTAR* low state data between 4–25 keV. The PN data are shown with green diamonds while the *NuSTAR* data are shown in blue hexagons (FPMA is shown with filled hexagons while FPMB is shown with empty hexagons). Panels A, B, C, D, and E show the five models tested. They include four absorption models and one blurred reflection model.

necessary to test if a complex absorbing scenario was possible. We could not obtain a fit with traditional absorption models that were statistically better than the IPC scenario in panel B.

Panel C of Figure 9 shows the 4–25 keV using a photoionized absorber XSTAR grid. This grid was constructed with properties described in Section 4.1 but with $A_{\text{Fe}} = 10$. With this fit, there is a deep residual at 6.7 keV, where the model drastically over-predicts the data. This can be solved by allowing the redshift of the XSTAR component free to vary. This produces the best-fit absorption model for these data. This is the only absorption model that could repro-

duce the shape of the spectra between 6 and 7 keV. However, this model requires the absorbing material to be in-flowing at $\sim 0.07c$.

Similarly, if we replace the neutral reflector with an absorbed PEXRAV component (Magdziarz & Zdziarski 1995) and also allow it to inflow, it produces a similar quality of fit as panel D (AICc = 372.8, $C - \text{stat}/\text{dof} = 349/328$). More interesting is that the inflow velocity is $\sim 0.07c$, the same as in the absorbing scenario. This is attributed to the prominent edge feature produced at ~ 7.1 keV by both the absorption and reflection spectra. This edge feature is redshifted to align with the steep drop in the hard spectrum of Mrk 1239 observed near 6.7 keV.

Material inflowing at these velocities is a highly unlikely scenario, as Mrk 1239 has a high Eddington ratio ($\lambda = 0.2 - 2$, Pan et al. 2021; Jiang et al. 2021; Gravity Collaboration et al. 2023). Thus, we would expect any material in our line of sight to be outflowing rather than inflowing, (but see e.g. Pounds et al. 2018). This scenario represents the only way these data can be fit absorption.

The final model tested for the hard band is a blurred ionized reflector (see Ballantyne et al. 2001; Miniutti & Fabian 2004; Ross & Fabian 2005). This is a reflection spectrum that is subject to the relativistic blurring effects near the SMBH. The most often implemented model is RELXILL (García et al. 2014; Dauser et al. 2013). This model contains all the same parameters as XILLVER (photon index, Γ ; iron abundance, A_{Fe} ; disc ionization, $\log \xi$, and inclination) plus and blurring parameters like the inner disc radius (r_{in}) and outer disc radius (r_{out}), black hole spin ($a = cJ/GM^2$, where M is the black hole mass and J is the angular momentum) and the emissivity profile. The emissivity profile dictates the disc illumination as a function of distance (r) and is dependent on the geometry of the inner disc and the corona. It is described by a broken power law ($\propto r^{-q}$) with index 1 ($q = q_{\text{in}}$) used prior to the break radius (r_{br}) and index 2 ($q = q_{\text{out}}$) after. We define the reflection fraction as the observed ratio of reflected to continuum flux between 0.1 – 100 keV. This scenario is often used to describe the spectral and timing properties of NLS1s (see Fabian et al. 2009b; Chiang et al. 2015; Gallo et al. 2013, Gallo et al. 2015; Jiang et al. 2019; Waddell et al. 2019). In Buhariwalla et al. (2020), the data were insufficient to constrain a realistic blurred reflection model. Specifically, the emissivity profile could not be constrained, yielding results that were difficult to interpret. The inner and outer emissivity index were fixed to a constant value of 3.

We have sufficient data quality to allow the emissivity profile to vary. However, initial tests find the break radius and q_{out} are degenerate. This is somewhat unsurprising as the emissivity profile is very difficult to constrain. The value of q_{out} we recover was consistent with the Newtonian value of $q_{\text{out}} = 2$, indicating the primary X-ray source is at a large

distance. The break radius is sufficiently high to be consistent with this scenario, so we fix $q_{\text{out}} = 2$. We test fixing $q_{\text{out}} = 3$ and find the AICc value increases by $\Delta\text{AIC} = 7.3$, indicating these values produce a similar result, but $q_{\text{out}} = 2$ is preferred with more than 95 per cent confidence. We note that when $q_{\text{out}} = 3$, the q_{in} value produced is consistent with what we report here, but the break radius becomes much smaller ($\sim 10 r_g$).

Initial fits always pegged the high energy cut-off at maximum, so this parameter was fixed to 300 keV. The inner radius is fixed at the innermost stable circular orbit, and the outer radius is fixed at $400 r_g$. The spin of the black hole is fixed to $a = 0.998$. The reflected photon index is linked to the intrinsic power law photon index, which is allowed to vary. The inclination, ionization parameter and iron abundance are also all free to vary.

The reflection scenario sufficiently models the spectral shape of the hard band, producing an AICc = 359.4. This is a better fit than the inflowing absorption model ($\Delta\text{AIC}_{D-E} = 8.4$), and it invokes a much more plausible scenario than ionized material in-flowing at $0.07c$.

4.3. Fitting the broadband, Pre-Flare Low State Spectra

Combining the best-fit soft band model with the best-fit hard band model allows us to explore how they might work together. The broadband model reads as ZTBABS*APEC + ZBREM + XILLVER + ZTBABS*(PO + RELXILL) and was fit across the 0.3 – 10 keV PN spectrum together with the 4 – 25 keV *NuSTAR* spectrum. The inclination was linked between XILLVER and RELXILL, and the reflection photon index for all components was tied to the power law photon index. The fit statistic for this model was $C - \text{stat}/\text{dof} = 429/408$, AICc = 468.6. Figure 10 shows the data, models and ratios.

We also tested different flavours of RELXILL models, including RELXILLLP for reflection with a lamppost geometry and RELXILLCP, for a variable density accretion disc and Comptonized continuum (see Dauser et al. 2022, for details). We find a worse fit for both, with a $\Delta\text{AIC} = 11.7$ and $\Delta\text{AIC} = 4.9$ for RELXILLLP and RELXILLCP, respectively. Thus, we continue with the standard flavour of relxill.

We tested whether un-linking the photon index between PN and *NuSTAR* affected the fit statistic. The $\Delta\text{AIC} = 2.1$, favouring the linked photon index. If we link the iron abundance between XILLVER, and RELXILL, the fit is worse by $\Delta\text{AIC} = 6.5$. The reflection fraction in the low state was calculated as the ratio between the blurred reflected flux and the power law flux between 0.1 – 100 keV. It was found to be $R = 2.4^{+1.3}_{-0.5}$. We note that Buhariwalla et al. (2020) struggled to find the reflection fraction with the available data because of the lack of power law contribution below 10 keV. In the absence of data below 10 keV, the power law component

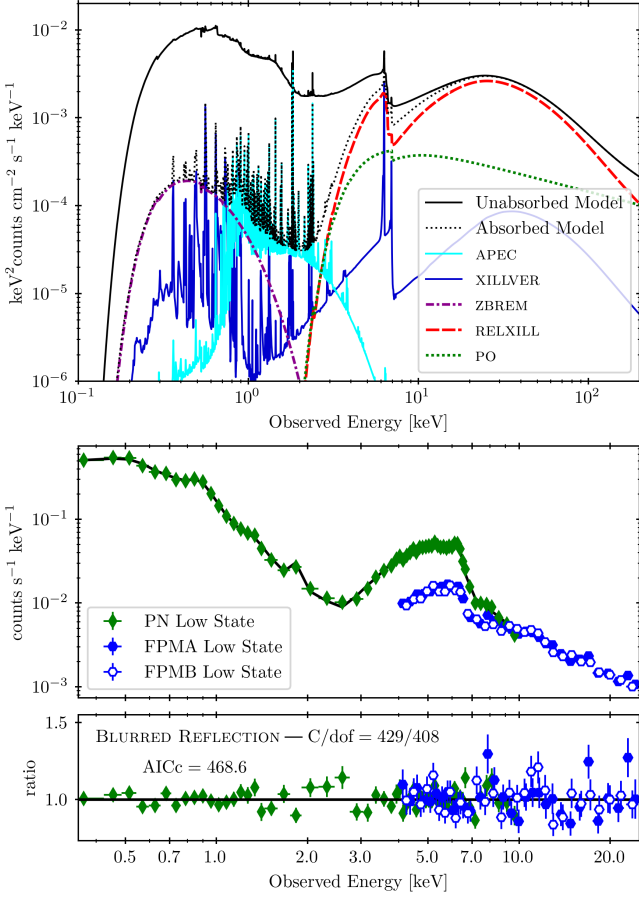


Figure 10. *Top panel:* The 0.1 – 200 keV low state model. Black solid and dotted lines show the unabsorbed and absorbed models, respectively. The individual emission components of the models are also shown. The bremsstrahlung (ZBREEM) component is shown with the dashed purple line, the photoionized component (XILLVER) is shown in dark blue, while the collisionally ionized component (APEC) in light blue. The AGN continuum is comprised of the primary emitter (PO) in the dotted green line, and the blurred reflection component (RELXILL) is shown with the dashed red line. *Middle panel:* The low state data. The 0.3 – 10 keV PN data is shown in green diamonds, the 4 – 25 keV *NuSTAR* spectrum is shown in blue hexagons FPMA and FPMB are shown with filled and unfilled hexagons, respectively. *Bottom panel:* The ratio of the blurred reflection fit, same labels as the middle panel. The data has been binned for clarity.

is negligible in the models, and only an upper limit can be estimated for the reflection fraction.

We also tested whether having the spin, inner disc radius, and cutoff temperature of the corona free affected the fit; they did not. The spin is constrained to $a > 0.6$, and leaving it free to vary did not improve the fit. Similarly, the inner radius was constrained to be $r_{in} < 4r_g$. Having the inner radius free did not impact the fit statistics. The cutoff temperature remained unconstrained. We thus left the spin, inner radius and cutoff temperature fixed to the values listed in Table 5.

We note there are intrinsic difficulties constraining reflection parameters without soft band data (see [Bonson & Gallo 2016](#), for details). Due to the nature of Mrk 1239, the intrinsic AGN emission in the soft band data is completely absorbed below 3 keV. Thus, we interpret the parameters carefully. As per [Bonson & Gallo \(2016\)](#), and similar works ([Choudhury et al. 2017](#); [Kammoun et al. 2018](#)), parameters such as photon index and inclination are relatively easy to measure. However, spin, q_{in} and $\log \xi$ are more difficult to recover accurately. Instead of focusing on the value of individual parameters, we will broadly interpret the physical scenarios.

Overall, the soft and hard band models come together quite well, considering they were developed independently. An interesting note about this model is that when the 10^{23} cm^{-2} absorber is removed from the AGN continuum (solid black like in Figure 10), much of the interesting soft band behaviour of this source is washed away. Simulating an 80 ks PN spectrum using this model can adequately fit the data using blurred reflection and a power law component, eliminating the need for extra soft band components. The simulated data, along with the observed data, can be seen in Appendix C.

4.4. Self-Consistent Spectral Fits including the flaring High-State

Next, we attempt to fit the 2021 high-state spectra with the best-fit model to the low-flux state (Section 4.3). Parameters that we expect to be constant or slowly varying were linked between the low and high states. These include all soft-band components, the spin, inclination, and ionization of the accretion disc. We allowed parameters that we expect to respond quickly free to vary. This includes the photon index, emissivity profile and normalization of the power law and reflection component. We find that the high state can be well fit by linking q_{out} and the break radius, allowing q_{in} , Γ , and normalization free. Figure 11 shows the best-fit models, data and ratios of this fit, while Table 5 shows the best-fit parameters. The corner plots for the MCMC error calculation can be seen in Appendix D. This model produced a fit of $C - \text{stat}/\text{dof} = 657/666$, $\text{AICc} = 706.6$. We also note the best-fit absorption model can not describe the 2021 flare with only photon index and normalization changing and has a $\Delta \text{AIC} = 66.5$, and the absorber must be inflowing at $\sim 0.11c$ for the high state (the low state still required inflow at $0.07c$).

The low state inner emissivity index was measured to be $q_{in,L} = 3.53 \pm 0.11$, while the high state was measured to be $q_{in,H} = 4.02^{+0.16}_{-0.15}$. We tested to see if this difference was due to the nature of the instruments used for the observation. This was done in two ways. First, we tested whether allowing q_{in} for the low state *NuSTAR* spectra to be separate from the low state PN spectra produced a significantly better

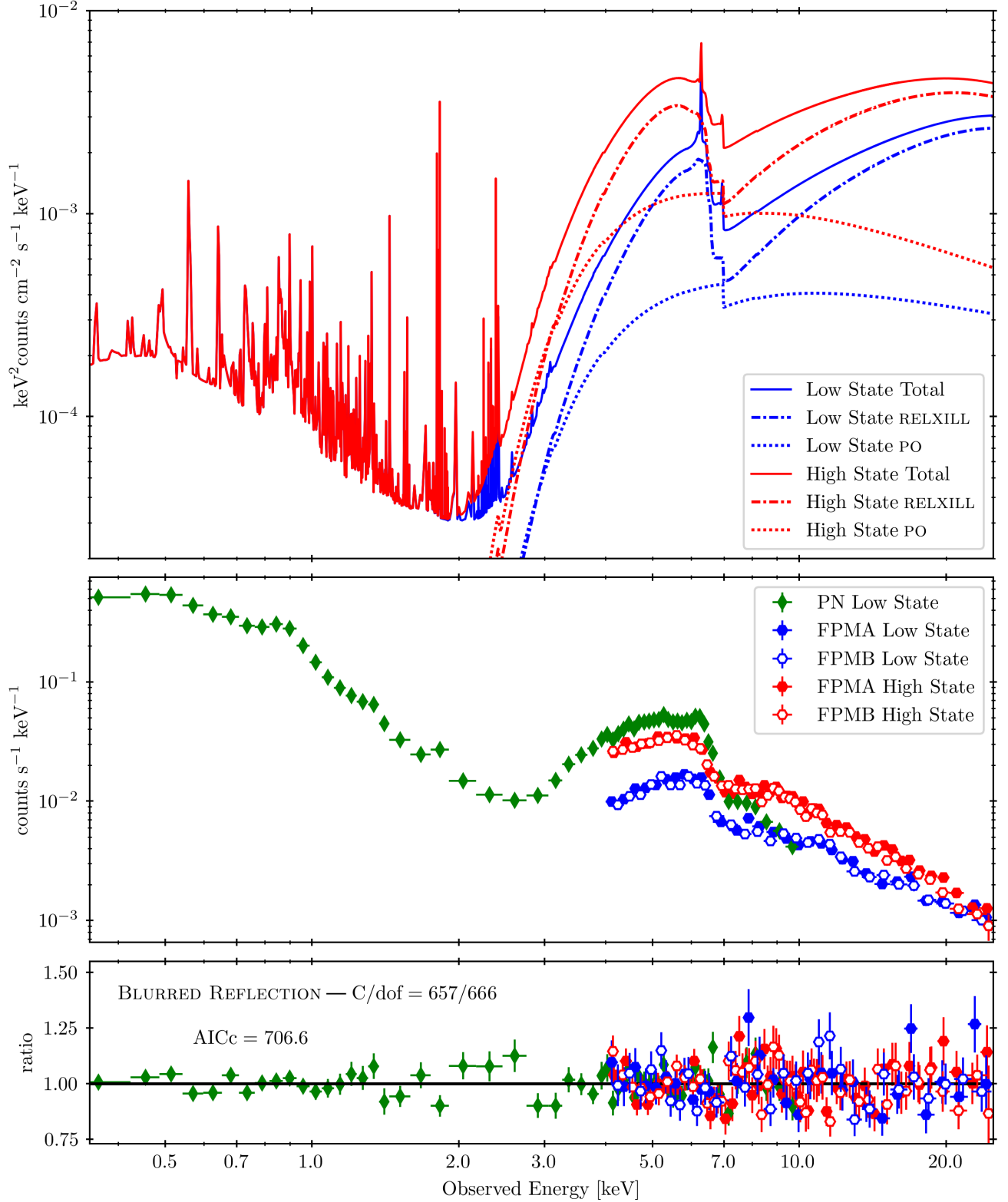


Figure 11. *Top panel:* The 0.3 – 25 keV total model for the low and high states are shown in the solid blue and red lines, respectively. The low and high state reflection (dot-dashed line) and power law (dotted line) components are also shown, as these are the only components that show variability between the low and high states. *Middle panel:* The low and high state data. The 0.3 – 10 keV PN data is shown in green diamonds, the 4 – 25 keV *NuSTAR* low state spectrum is shown in blue hexagons, and the 4 – 25 keV *NuSTAR* high state spectrum is shown in red hexagons. FPMA and FPMB are shown with filled and unfilled hexagons, respectively. *Bottom panel:* The ratio of these data fit with the blurred reflection model, with the same labels as the middle panel. The data has been binned for clarity.

(1)	(2)	(3)	(4)	(5)
Physical Component	Model Component	Model Parameter	Low State	High state
Neutral absorber	ZTBABS	N_H [$10^{22}/\text{cm}^2$]	0.73 ± 0.05	
Collisionally Ionized Component	APEC	kT [keV]	0.80 ± 0.03	
		Abundance [solar]	1^f	
		norm	$3.2 \pm 0.3(\times 10^{-4})$	
Bremsstrahlung Emission	ZBREM	kT [keV]	0.23 ± 0.02	
		norm	$1.6 \pm 0.2(\times 10^{-3})$	
Photoionized Emission	XILLVER	$\log \xi$ [$\text{erg cm}^{-2} \text{s}^{-1}$]	$1.21^{+0.11}_{-0.12}$	
		Inclination [deg]	17^l	
		A_{Fe} [solar]	1^f	
		Γ	2.44^l	
		norm	$5 \pm 1(\times 10^{-6})$	
Neutral absorber	ZTBABS	N_H [$10^{22}/\text{cm}^2$]	$29.2^{+1.3}_{-1.4}$	
Blurred reflector	RELXILL	q_{in}	3.53 ± 0.11	$4.02^{+0.16}_{-0.15}$
		q_{out}	2^f	
		r_{Br} [r_g]	46^{+11}_{-7}	
		r_{in} [r_g]	$1.2^{f,*}$	
		r_{out} [r_g]	400^f	
		spin	0.998^f	
		Inclination [deg]	17^{+4}_{-6}	
		$\log \xi$ [$\text{erg cm}^{-2} \text{s}^{-1}$]	2.6 ± 0.2	
		A_{Fe} [solar]	> 9	
		E_{cut}	300^f	
		Γ	2.43^l	2.83^l
		norm	$4.1^{+1.0}_{-0.9}(\times 10^{-4})$	$39^{+17}_{-10}(\times 10^{-4})$
		Γ	2.44 ± 0.07	$2.82^{+0.09}_{-0.04}$
		norm	$1.5 \pm 0.4(\times 10^{-3})$	$8.9^{+1.4}_{-1.3}(\times 10^{-3})$
Intrinsic Power Law	POWERLAW	Γ	2.44 ± 0.07	$2.82^{+0.09}_{-0.04}$
		norm	$1.5 \pm 0.4(\times 10^{-3})$	$8.9^{+1.4}_{-1.3}(\times 10^{-3})$
Calibration Constatnts	FPMA		$1.01^{+0.04}_{-0.03}$	
	FPMB		1.03 ± 0.04	1.02 ± 0.03

Table 5. Best fit parameters for the low and high state models. Column (1) lists the physical description of the XSPEC component listed in Column 2. Column (3) outlines the model parameters from each model component. Columns (4) and (5) show parameter values for the low state and high state, respectively. If a parameter is blank in Column (5), that value is linked between the low and high states. The parameters with superscript f have been fixed to the displayed value, while the parameters with the superscript l have been linked to the same parameter in a different model component within the model. (*) This is fixed to the innermost stable circular orbit, which for a maximal spinning black hole is $1.2 r_g$.

fit. This gave $\Delta\text{AIC} = 4.0$, favouring the separate indices. However, the separate q_{in} values were comparable. Next, we linked all the emissivity profile parameters between the low and high states. This produced a significantly worse fit, with a $\Delta\text{AIC} = 80.3$, indicating that separate inner indices are strongly preferred between the low and high states. Together, this suggests that the change in the emissivity profile is required by the data rather than a result of the different instrumentation.

While it is difficult to state properties of the accretion disc with these data confidently, we can infer some things about the regions that produced the reflection spectra. Based on the emissivity profile, we are seeing limited light bending effects as compared to other sources like MCG-6-30-15 (Brenneman & Reynolds 2006) and 1H 0707 – 495 (Fabian et al. 2012), which have steep inner emissivity profiles (e.g. $q_{in} > 6$). Instead, our value is closer to $q_{in} \sim 4$, indicating we are viewing reflection off the accretion disc at some distance from the SMBH. We do not speculate why as there could be a myriad of factors (different spin, inner radius, absorption effects, etc.); we only speculate on why the inner emissivity index may have changed during the flare.

Overall, our analysis demonstrates the differences between the low-flux and flaring levels can be described by changing the reflection fraction and overall flux of the power law. The low state reflection fraction was measured to be $R_L = 2.4^{+1.3}_{-0.5}$, while the high state reflection fraction was measured to be $R_H = 1.6^{+0.6}_{-0.4}$. The low state photon index was measured to be $\Gamma_L = 2.43 \pm 0.06$ and the high was $\Gamma_H = 2.82^{+0.09}_{-0.04}$. The physical motivations of this flare will be discussed in the next section.

5. SPECTRAL VARIABILITY ANALYSIS

5.1. Principal Component Analysis Based on New Best-fit X-ray Model

In Section 3.4, we established that the best-fit ionized partial covering model from Buhariwalla et al. (2020) could not adequately describe the variability of Mrk 1239 despite providing a good fit to the spectrum. Here, we will perform a principal component analysis based on the best fit spectral model discerned in Section 4 to determine if it could reasonably describe the rapid and long-term variability. The main difference between the new model and that of Buhariwalla et al. (2020) is that the covering fraction of the neutral absorber is 100%, indicating no AGN continuum leaking into the soft band.

Twenty PN spectra and forty *NuSTAR* spectra were simulated like in Section 3.4. The twenty PN spectra had the normalization of the power law and blurred reflection component change such that the resultant spectra had count rates ranging from $\sim 0.4 - 0.7 \text{ count s}^{-1}$, consistent with the count rate variation seen in the PN light curves.

For the forty *NuSTAR* spectra, twenty had power law and reflection normalization changing by $\sim 20\%$, representing the low state and the 2019 data. The other twenty had variable power law and reflection normalization, changing by a factor of 5 to represent the flaring data. The 4 – 30 keV count rates ranged from $0.15 - 0.75 \text{ count s}^{-1}$, representing the variability in the *NuSTAR* light curves.

This was somewhat of a naive approach to simulating the spectral variability as we only account for a monotonic change in the AGN continuum. The reflection fraction, photon index, and inner emissivity index remain constant throughout. These are parameters we know to vary during the *NuSTAR* flare. However, this approach is sufficient for the first-order approximation we are attempting here. Figure 12 shows the first principal component for the PN and *NuSTAR* data along with the first principal component for the simulated data.

With this model, the simulated PN spectrum matches the observed data well. There is a slight disagreement around 3 keV and around the location of the broad iron line, which could be improved upon by complicating the model (e.g. varying the reflection fraction or ionization parameter). The simulated *NuSTAR* principal component matches the overall data well, suggesting this simplistic model for the variability is responsible.

Moreover, the model also reproduces the negligible variability below 3 keV. The easiest explanation for the consistent nature of the soft band is that it is physically large. This was the interpretation used in Buhariwalla et al. (2020), where the CIE originated from regions of star formation within the galaxy. A very long timeline would be needed to explore variations of three ionized components making up the soft band. To attempt to examine the variability of the three soft band components with the current data, we fitted the 0.3 – 2 keV PN spectra, the 2001 MOS, 2007 *Suzaku* XIS, and the 2019 *Swift* XRT spectra with the same model described in Section 4.1. All parameters were linked between epochs, and only the normalization of each component was allowed to fluctuate. This was done to explore any possible variation of the strength of each component across the 20 years of data. The 0.2 – 2 keV luminosity of each component was measured using CLUMIN. The snapshot *Swift* observations were not included in this analysis.

Figure 13 shows the unabsorbed luminosity for each component of the soft band at each epoch. We compare the measurements to the error-weighted mean luminosity over all epochs. We can see that the APEC and ZBREM components have roughly the same unabsorbed luminosity. However, when absorbed, the luminosity of the APEC component is ~ 0.7 dex lower, making its observed luminosity the lowest of the three components.

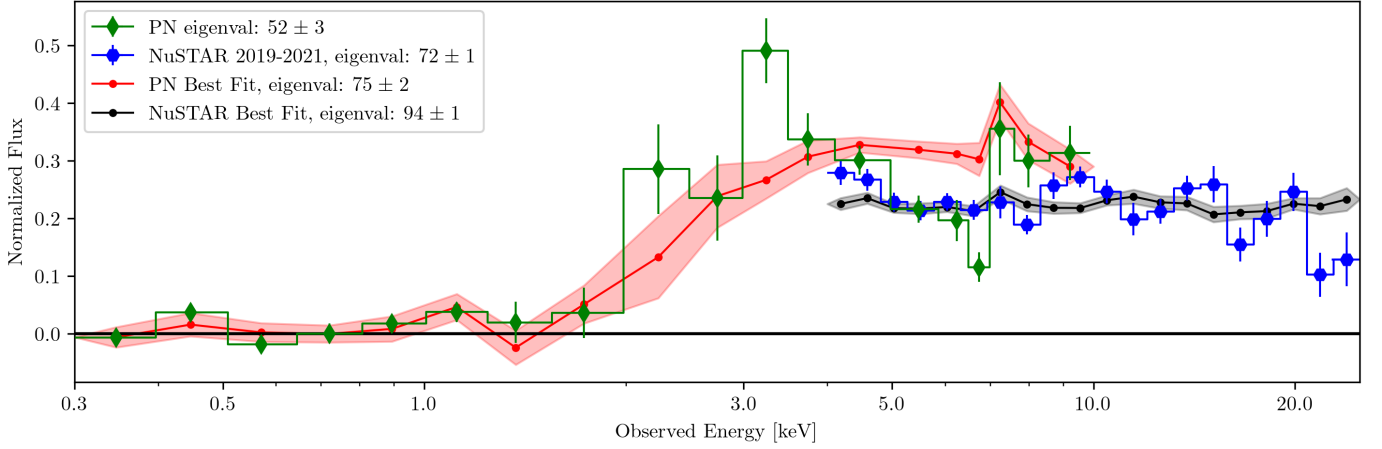


Figure 12. The observed first principal component for the PN and *NuSTAR* data are shown in green diamonds and blue hexagons, respectively. The simulated first principal component based on the best-fit model for the PN and *NuSTAR* data is shown with the red-shaded and grey-shaded regions, respectively. We can see that the general trends in variability are better reproduced using this model.

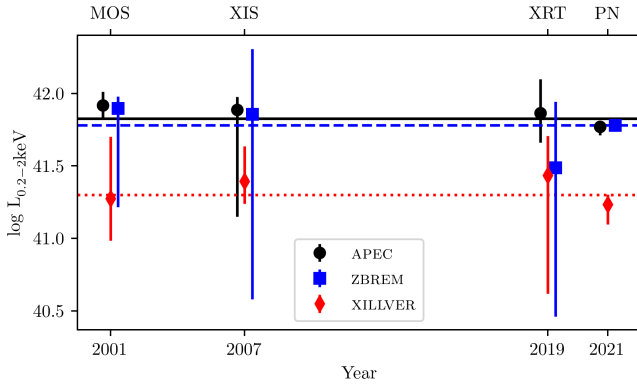


Figure 13. The 0.2 – 2 keV luminosity of the APEC (black circle), ZBREM (blue square), and XILLVER (red diamond) component at each epoch that spectral data is available for. The black solid line shows the error weighted mean luminosity for the APEC component, the blue dashed line for the ZBREM component and the red dotted line for the XILLVER component. The lower axis outlines the year of the observation, while the upper axis shows the instrument used to observe. A small horizontal offset in the date is introduced for visual clarity.

The APEC component is the only one well-constrained at every epoch. The reason for this is likely because the three instruments used all have adequate effective area and calibration at approximately 0.9 keV. This is where the main feature of the APEC component is evident. This feature is present above whatever continuum is present in this object. The ZBREM is relatively strong in all epochs; however, it is hard to accurately constrain its strength as it peaks at very low energies, and only the high energy tail is observable.

Based on these spectral data, we see no evidence of variability in any of the individual components that comprise the soft band. A long timeline and high-quality data would be needed to probe any subtle changes fully.

5.2. The Rapid Flaring Event Captured by *NuSTAR*

To investigate the flaring event caught with *NuSTAR*, we subdivided the low and high-flux intervals into two and four spectra, respectively (see Figure 14). Each subdivided spectra contained 2400 – 6600 counts summed between FPMA and FPMB. They averaged ~ 25.6 ks and ~ 12.4 ks total exposure time (~ 50 ks and ~ 25 ks duration) for the low and high states, respectively. These spectra were fit along with the average high, low and PN spectra using the parameters found from the best-fit model. For each spectrum, we allowed only the photon index, reflection fraction, and power law normalization to vary. We report these parameters in Figure 14. The empty blue hexagons indicate the average low state value, and the filled red hexagons show the average high state value. The empty black circles show the subdivided low-state values and the filled black circles show the subdivided high-state values.

The luminosity of the power law component increases for the first 150 ks before dropping slightly after the flare peaks. The reflection fraction in the low state decreases as the power law luminosity increases. During the first 50 ks, the system is in a true low state, as we saw in 2019. Then, between 50 and 100 ks, the corona exhibits a small flare and increases in brightness. Correspondingly, the reflection fraction is reduced.

Between 100 and 125 ks, the main flare begins, and the power law luminosity increases again. However, the reflection fraction initially remains constant, indicating that emission from the disc has increased. The flare peaks just before 150 ks. This corresponds to the largest power law luminosity and the lowest reflection fraction. The reflection fraction remains low as the power law luminosity begins to fall off after the flare before increasing slightly by the end of the *NuSTAR* observation.

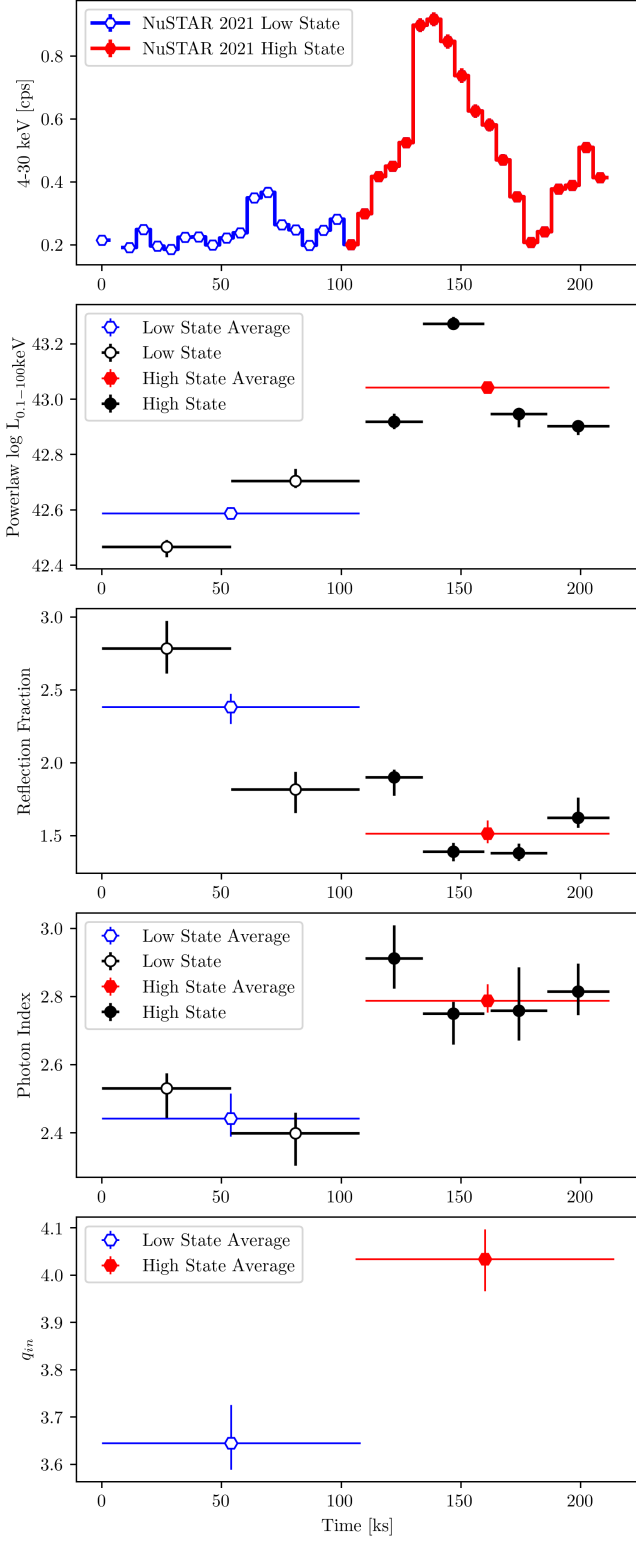


Figure 14. *Top panel:* NuSTAR 4 – 10 keV light curve. *Second panel:* The log 0.1 – 100 keV luminosity of the power law component. *Third panel:* Reflection fraction calculated using the observed 0.1 – 100 keV luminosity of each component. *Fourth panel:* The photon index, and *Bottom panel:* The inner emissivity index for the average low and high states.

The reflection fraction is not obviously inversely correlated with the power law on the short time scales. This would be the behaviour expected if the blurred reflection component was constant on rapid time scales; changes in the power law luminosity would be the only component driving the changes in reflection fraction. However, this is not what is observed. At some point, photons emitted by the corona reflect off the disc and then are remitted out of the system. This might indicate some delay between the power law and reflection components, which is an expected consequence of blurred reflection (Fabian et al. 2009b; Zoghbi et al. 2010; Wilkins et al. 2014). Unfortunately, we do not have the data quality to probe on finer time scales.

The rapid flare seen over the 4 – 30 keV band points to a significant level of intrinsic AGN variability in Mrk 1239 that is comparable to other NLS1s. Figure 14 reveals several observed flux-related parameter changes. We can see that the change between the low and high states happened quickly for the photon index and inner emissivity index. This change in Γ between the low and high states suggests that the physical conditions in the corona change during the NuSTAR observation. The photon index of a corona is determined by its Compton- y parameter (see: Longair 1992; Rybicki & Lightman 1979; Fabian et al. 2015), which is dependant on the temperature (T_e) and the optical depth (τ_e) of the emitting plasma. Presumably, either or both of these parameters may have changed during the flare. It is difficult to isolate the interesting parameters as they are degenerate. Measurement of the cut-off energy would be beneficial (e.g. Wilkins et al. 2014; Wilkins et al. 2022), but this could not be constrained with the current data.

The change in the inner emissivity index is the opposite of what we might expect from a corona with lamp-post geometry. In a lamp-post geometry, the corona is considered a point source at some height h , above the accretion disc. If the height of the corona changes by moving to a larger h , then the number of continuum photons escaping the system would increase, leading to an increase in flux and a decrease in reflection fraction, as we see in Mrk 1239. However, this increase in height would lower the inner emissivity index as fewer continuum photons would be incident on the inner disc (Wilkins & Fabian 2012). Furthermore, under a lamp-post geometry, the break radius we observe suggests a coronal height of $\sim 50 r_g$ (Wilkins & Fabian 2012). At this height, we would not expect to see the high reflection fraction we observe in this AGN (Gonzalez et al. 2017).

The increase in photon index, decrease in reflection fraction and increase in the inner emissivity index mirror the behaviour of Mrk 335 during a proposed jet launching event (Wilkins & Gallo 2015). The changes in the parameters we see in Mrk 1239 are far less extreme but do follow the same trend. This could indicate a vertically extended corona,

which would produce an emissivity profile very similar to a broken power law, with the inner emissivity index being slightly steeper than the outer index (Wilkins & Fabian 2012). That is consistent with the emissivity profile we measured in Mrk 1239.

6. DISCUSSION

6.1. The Origin of the Soft X-ray Emission Components

Unlike most NLS1s, the central engine of Mrk 1239 is hosted in an elliptical (König et al. 2009) or compact galaxy (Mazzarella & Balzano 1986). It has been classified as unbarred and bulge-dominated (Husemann et al. 2022). It is known that the hot gas in such galaxies can produce emission detectable in the soft band related to their hot interstellar medium (ISM) (Fabbiano 2012). In particular, there are well-known relations between the X-ray luminosity and the optical and infrared bands. Here, we compare the soft band luminosity of Mrk 1239 to that of other S0 and elliptical galaxies.

The luminosity of the ISM in the 300 kpc surrounding the massive elliptical galaxy, NGC 4636, is $L_{0.5-4.5\text{keV}} = 10^{41.9} \text{ erg s}^{-1}$ (Matsushita et al. 1998). NGC 4636 has a total mass of $9 \times 10^{12} M_{\odot}$ (Matsushita et al. 1998), and a stellar mass of $7 \times 10^{11} M_{\odot}$ (Mathews 2021). The X-ray emission of the ISM is spatially resolved. Its RGS spectra can be fit with an APEC component whose temperature increases with radius from 0.53 keV to 0.71 keV (Xu et al. 2002). The temperatures observed in NGC 4636 are comparable to what we observe in Mrk 1239. The 0.5 – 4.5 keV luminosity of just the soft band components in Mrk 1239 is $L_{0.5-4.5\text{keV}} = 10^{41.7} \text{ erg s}^{-1}$, 0.2 dex less than NGC 4636. However, Mrk 1239 is relatively isolated and has a much smaller stellar-mass ($M_* = 1.5 \times 10^9 M_{\odot}$ Pan et al. 2019; $M_* = 1.0 \times 10^{10} M_{\odot}$ Smirnova-Pinchukova et al. 2022) as compared to NGC 4636 ($M_* \sim 10^{12} M_{\odot}$ Mathews 2021).

The $L_X - L_B$ relation found in ellipticals shows that at higher blue luminosities, the X-ray luminosity also increases (Diehl & Statler 2007). To compare Mrk 1239 to the sample of elliptical galaxies, we first estimate the B-band luminosity to be $L_B = 10^{10} L_{\odot,B}$ based on an SDSS u magnitude $u = 16$ and a luminosity distance of $D_L = 86 \text{ Mpc}$ (Sani et al. 2010). The absorbed X-ray luminosity over 0.3 – 5 keV of the collisional and constant continuum components combined were $L_{X,T} = 10^{41.7} \text{ erg s}^{-1}$ ($L_{X,\text{CIE}} \sim 10^{41.2}$, $L_{X,\text{CC}} = 10^{41.5} \text{ erg s}^{-1}$, for collisional and constant continuum components, respectively). Comparing to figure 4 of Diehl & Statler (2007), we see that the measured L_B indicates that the luminosity of the soft band components in Mrk 1239 should be of order $L_X = 10^{40} - 10^{41} \text{ erg s}^{-1}$. The observed values are greater than expected. If we explore the unabsorbed luminosity the discrepancy increases. The unabsorbed luminosity of the collisional component becomes $L_{X,\text{CIE}} \sim 10^{41.8} \text{ erg s}^{-1}$, while the unabsorbed

luminosity of the constant continuum component becomes $L_{X,\text{CC}} = 10^{42.7} \text{ erg s}^{-1}$. The total luminosity then becomes $L_{X,T} = 10^{42.8} \text{ erg s}^{-1}$.

Similar relationships exist between the stellar luminosity, as measured by the K -band, and the X-ray luminosity of the ISM of elliptical galaxies (Boroson et al. 2011). Repeating the above exercise with K magnitudes from 2MASS, we take $K = 9.6$, resulting in $L_K = 10^{11.4} L_{\odot,K}$. Comparing this to figure 2 of Boroson et al. (2011), we see that the luminosity of each X-ray component and the total luminosity of Mrk 1239 is greater than the hot gases, low mass X-ray binaries (LMXB), and nuclear emission in all of the elliptical galaxies probed.

We note that the B and K -band luminosities of Mrk 1239 have not been corrected for AGN emission, and thus, the discrepancy between the expected X-ray luminosity and what we observe is only a lower limit here. As such, the discrepancy here indicates that the soft band emission we see in Mrk 1239 does not originate purely from hot gases often seen in elliptical galaxies. Instead, this emission must be associated with some process indirectly powered by the AGN.

The soft X-ray emission in Mrk 1239 appears to originate from three distinct components. Based on the *Chandra* image of Mrk 1239, we know that the soft X-ray emission originates within 500 pc of the central engine and is asymmetric (Buhariwalla et al. 2023).

These soft band components may be common in all AGN with radio jets and are only visible in Mrk 1239 due to the heavy absorption present. The unabsorbed AGN continuum luminosity between 0.2 – 2 keV is $\log L_{0.2-2\text{keV}} = 43.2 \text{ erg s}^{-1}$. The luminosity of the bremsstrahlung component in the same band ($\log L_{0.2-2\text{keV}} = 41.8 \text{ erg s}^{-1}$) is less than 4 percent of the AGN luminosity. All three soft band components would represent ~ 8 percent of the AGN luminosity in the soft band. A simulated spectrum with no continuum absorption and the three soft band components can be fit with just the continuum contributions from RELXILL and PO (see Appendix C). This indicates that these components could very well be present in other galaxies and simply be overwhelmed by the central engine. We can see this in the top panel of Figure 10, where the unabsorbed model is ~ 1 dex above most emission lines and ~ 2 dex above the soft band continuum.

6.1.1. The Photoionized Emission

The photoionized component was modelled with XILLVER in the CCD spectra, whereas the photoionized component in the RGS spectra was modelled with an XSTAR grid (Buhariwalla et al. 2023). The reason why XILLVER is a poor fit in the RGS spectra is that it is at a sufficiently high density ($10^{15}/\text{cm}^3$), the forbidden line of the O VII triplet is sup-

pressed. In the PN spectra, we cannot resolve any individual line in the soft band, thus XILLVER appears adequate.

If we very closely examine the ratio of models 7 and 6b (ZPCFABS*APEC+ZBREM+XSTAR/XILLVER, for 7/6b, respectively), the discrepancy between the models lies mostly between 0.4 – 0.6 keV. This is the location of the two most prominent photoionized features found in the RGS spectrum, the O VII triplet and N VII line. While XILLVER does not reproduce the O VII triplet expected in this energy band, it is at such low resolution that all three O VII lines blend together in addition to the N VII line. We note that Buhariwalla et al. (2023) were underfitting the N VII line at 25 Å (0.495 keV) with their best-fit model. Thus, XILLVER is better at accounting for the emission in this narrow band. The true nature of the photoionized material thus must lie somewhere in between the XSTAR and XILLVER models.

The physical location of the photoionized material is at some distance greater than the dust sublimation radius, and it is outflowing at a velocity of $\sim 660 \text{ km s}^{-1}$ (Buhariwalla et al. 2023). We see no evidence of absorption of this component, indicating that we have a clear line-of-sight to the site of the photoionized emitter. The photoionized emitter could be originating from an outflow on torus scales. We note that the photoionized emitter is also responsible for fitting narrow features in the Fe K α band. This assumes that the region responsible for producing the Fe K α is the same as producing the O VII triplet emission.

Understanding the continuum photoionizing the gas is imperative to determine the location and nature of the photoionized emission. With the RGS data, we were unable to distinguish different illuminating sources. However, the PN data can offer some insight. There is no fit improvement by allowing the XILLVER component to have Γ free and distinct from the power law continuum. Also, fixing the photon index of the photoionizing continuum to the value of the power law continuum is indistinguishable from fixing at the fiducial value of $\Gamma = 2.5$. We can, however, constrain the photoionizing continuum photon index to be $\Gamma > 2.2$. This indicates that the primary X-ray continuum is responsible for ionizing the photoionized emission, and thus, there must be a relatively clear line of sight between the corona and the photoionized material. Furthermore, there must be a clear line of sight between the photoionized material and the observer. To accomplish this, the neutral absorber must be asymmetric. Details of the geometry of the system will be discussed further in Section 6.2.

6.1.2. The Collisionally Ionized Emission

Based on the best-fit model, the CIE (APEC) component is absorbed. This results in an intrinsically brighter APEC component than was previously reported in Buhariwalla et al. (2020). The new higher value of $L_{2-10\text{keV}}$ results in a new

SFR estimate between $25 - 35 \text{ M}_{\odot} \text{ yr}^{-1}$ (Franceschini et al. 2003). Based on $L_{0.5-2\text{keV}}$, the SFR would be in excess of $100 \text{ M}_{\odot} \text{ yr}^{-1}$ (Ranalli et al. 2003).

It becomes much less likely that this collisionally ionized emission is originating in regions of star formation as this is orders of magnitude greater than the SFR predicted in other band passes [PAH measurements, $\leq 7.5 \text{ M}_{\odot} \text{ yr}^{-1}$, (Ruschel-Dutra et al. 2016); SED fitting, $3.47 \pm 0.26 \text{ M}_{\odot} \text{ yr}^{-1}$ (Gruppioni et al. 2016); IR measurement, $2.1^{+0.5}_{-0.4} \text{ M}_{\odot} \text{ yr}^{-1}$, (Smirnova-Pinchukova et al. 2022)].

An alternative could be the shock heating of material as it is pushed into the ISM by the jet or other outflow mechanisms present in this galaxy. Modelling the soft band with a plane parallel shocked plasma model, PSHOCK, produces a fit of equal quality as with APEC ($\Delta\text{AIC} = 5$, favouring APEC).

6.1.3. The Featureless Continuum

There is a constant featureless continuum component evident in the soft band. In Buhariwalla et al. (2020), this component was attributed to the leaky absorber permitting AGN continuum from the central engine to contaminate the soft band. Our timing analysis has demonstrated the AGN varies significantly, and any leaked emission should also vary. However, the soft band does not exhibit such behaviour. Instead, we can fit the featureless continuum using either a bremsstrahlung (ZBREM) or a black body (ZBB) component, with the bremsstrahlung component being preferred statistically. This component was not detected in the RGS spectra. The flux between a 0.5 – 1.77 keV (7.3 – 24.7 Å) of the ZBREM component in the PN spectra is $\sim 1.2 \times 10^{-13} \text{ erg cm}^{-2} \text{ s}^{-1}$. The flux of the RGS background in this region is $\sim 6 \times 10^{-13} \text{ erg cm}^{-2} \text{ s}^{-1}$, or approximately five times brighter. Thus, the null detection of the constant continuum component in the RGS was likely a sensitivity issue.

It is unlikely that the origin of the constant continuum component lies with an actual bremsstrahlung emitting plasma. Firstly, the model component, ZBREM, relies on a thermal distribution of electrons (Kellogg et al. 1975), while the most probable location for a bremsstrahlung emitting plasma to exist in an AGN is inside a radio jet. Those electrons, however, would have a non-thermal distribution and thus would produce a non-thermal spectrum.

If we consider it a thermal bremsstrahlung plasma, then we find this is also not plausible. The temperature of the ZBREM component of $kT \sim 0.2 \text{ keV}$. The dominant continuum process of plasma at that temperature would not be bremsstrahlung radiation, but rather radiative recombination and/or 2-photon continuum (Böhringer & Werner 2010). These are the dominant continuum processes in APEC at this low temperature. We attempted to fit the soft band with two collisionally ionized components. The problem with this sce-

nario is that at low temperatures, emission lines dominate over all continuum processes (Böhringer & Werner 2010). Thus, to explain the presence of the constant continuum component using only collisional plasma, we would require the abundance of that plasma to be primordial, as this would effectively remove all emission lines. This is allowed by the data but stretches the imagination as to how such a plasma could exist.

Another option is that the origin is thermal emission from warm material. The temperature of the black body is $kT \sim 90 \text{ eV}$ ($T \sim 10^6 \text{ K}$). This is an order of magnitude hotter than we would expect for the accretion disc of an SMBH (Hickox & Alexander 2018). Even if Mrk 1239 was host to an exceptionally hot accretion disc, we would not expect to see it directly as it would also be obscured through the $N_H = 10^{23.5} \text{ cm}^{-2}$ absorber and thus not visible.

A final possible explanation for the excess emission is calibration issues between the RGS and PN instruments. There is a known correction needed between these instruments (See appendix B of Grafton-Waters et al. 2023, for details). However, we attempted to mitigate these effects by ignoring PN data below 0.5 keV , and we found that the excess emission was still present.

It is difficult to say anything more based on these data and deeper observations of Mrk 1239 with instruments like *Arcus* (Smith et al. 2019) and *Athena* (Nandra et al. 2013) to explore the soft band more fully.

6.2. The Geometry of Mrk 1239

In this work, we estimate the inclination of the accretion disc to be $\sim 17^\circ$, based on the blurred reflection model. The inclination of the torus was measured to be $\sim 6^\circ$ (Lakićević et al. 2022), which was consistent with the measurements of inclination of the broad line region (7° , Zhang & Wu 2002; 11° , GRAVITY Collaboration et al. 2024). We conclude that we are observing the system virtually face-on. The neutral absorber is unlikely to be directly associated with the torus at this inclination, as it would have to be nearly spherical. The opening angle of the broad line region was measured to be $\sim 42^\circ$, by GRAVITY Collaboration et al. (2024). If we assume that the torus is a natural evolution of the BLR (Koshida et al. 2014; Minezaki et al. 2019; Gallo et al. 2023) then the opening angle of the torus must be similar to $\sim 42^\circ$.

Two polarization regions are present in Mrk 1239, one associated with the dust in the broad line region (Goodrich 1989), the other associated with polar dust (Batcheldor et al. 2011; Lakićević et al. 2022). The polar dust region is responsible for the bulk of the polarization seen in the optical spectrum of Mrk 1239. This dust could be associated with the dust causing the attenuation. Furthermore, it could be associated with the IR bump due to hot dust that is present in Mrk 1239 (Rodríguez-Ardila & Mazzalay 2006). This dust,

however, is not hot enough to contribute to the featureless continuum we see in Mrk 1239.

Rodríguez-Ardila & Mazzalay (2006) measure an extinction of $E(B - V) = 0.54$, in the inner few $\sim 100 \text{ pc}$ of the central engine in Mrk 1239. Based on the dust-to-gas ratio of obscured quasars (Jun et al. 2021), this results in a column density of $1 - 4 \times 10^{22} \text{ cm}^{-2}$. The obscurer measured by Pan et al. (2021) close to the central engine had an extinction of $E(B - V) = 1.6 \pm 0.1$, which resulted in a column density between 4×10^{22} and $1 \times 10^{23} \text{ cm}^{-2}$. This is closer to the column density we measure in the X-ray regime ($\sim 3 \times 10^{23} \text{ cm}^{-2}$). The discrepancy could be due to uncertainty in the dust-to-gas ratio used to infer the column density of the optical obscurer.

Assuming a BH mass of $2.6 \times 10^6 M_\odot$ (Marin 2016; Gravity Collaboration et al. 2023), the Eddington luminosity is $33 \times 10^{43} \text{ erg s}^{-1}$. During the low state, the unabsorbed $0.1 - 100 \text{ keV}$ luminosity of the central engine is estimated to be $\sim 7 \times 10^{43} \text{ erg s}^{-1}$. Using this as a proxy for the bolometric luminosity gives an Eddington ratio of $\lambda = 0.2$. This is consistent with the value found by Jiang et al. (2021). Based on these values, we expect the absorbing material in Mrk 1239 to fall within the forbidden region of the $N_H - \lambda$ plane (Ishibashi et al. 2018). Thus we would expect the neutral absorbing material to be outflowing, which has been observed at $\sim 1000 \text{ km s}^{-1}$ (Pan et al. 2021). Comparing the absorbed and unabsorbed luminosity of the central engine, we find that $\sim 6 \times 10^{43} \text{ erg s}^{-1}$ are absorbed by the neutral material.

It seems this neutral absorber is asymmetric, extending much further on one side of the central engine than the other. Assuming this neutral material is what is crashing into the ISM, creating the collisionally ionized and accountant continuum emission, then this asymmetric cloud is consistent with the asymmetric soft emission that we see in the *Chandra* image of Mrk 1239 (Buhariwalla et al. 2023).

The outflowing velocity of this cloud is comparable to the velocity measured from the forbidden O VII line (Buhariwalla et al. 2023), suggesting a possible common origin. However, as discussed in Section 6.1.1, the photoionized emitter must have a clear line of sight to both the central engine and the observer, suggesting they are physically distinct. If we assume that the photoionized absorber is being blown off of the top of the torus at $\sim 45^\circ$ (GRAVITY Collaboration et al. 2024), then the resultant rest frame velocity of the photoionizing material would be $\sim 1000 \text{ km s}^{-1}$. The velocity would be different depending on the location on the torus that the PIE originates from. If the emitting region was tilted towards us as seen in Figure 15, then the rest frame outflow velocity might be closer to $\sim 800 \text{ km s}^{-1}$. If the PIE was located on the exact opposite side of the torus, tilling away

from us, then the outflow velocity might be closer to $\sim 1300 \text{ km s}^{-1}$.

Compact steep spectrum radio sources (CSS) may be young radio-loud galaxies trying to push their way out of the central region (Fanti et al. 1990; O’Dea 1998). The outflow velocity of these objects is typically $\sim 2000 \text{ km s}^{-1}$ (Fanti et al. 1990). In the radio, Mrk 1239 has a steep spectral slope (Berton et al. 2018; Järvelä et al. 2022) and it is incredibly compact. About 90% of the radio emission is contained within the central ~ 10 s of parsec (Doi et al. 2015). However, the jets are subsonic and not well collimated and instead might be considered a low-luminosity compact source whose radio jets have become disrupted or frustrated by the ISM and other material surrounding the central engine (Kunert-Bajraszewska et al. 2010; Doi et al. 2015; Järvelä et al. 2022).

The kinetic energy of the jet is estimated to be $\sim 10^{43} \text{ erg s}^{-1}$ (Doi et al. 2015). The bolometric luminosity of the collisional material (collisionally ionized and bremsstrahlung) is $10^{43} \text{ erg s}^{-1}$ which implies that $\sim 100\%$ of the jet kinetic energy is required to produce the collisional luminosity that we see in Mrk 1239. While the jet may provide some kinetic energy to the outflowing material, it is unlikely to be the sole contributor.

Figure 15 shows our proposed central engine geometry for Mrk 1239. The system is viewed virtually face-on (fiducial inclination of 15°) and contains all the standard components for an AGN (corona, accretion disc, BLR, torus). Where Mrk 1239 differs from the typical Type I galaxy is the massive asymmetric neutral absorber that is crashing into the ISM. The radio jet or radiatively driven outflow (or both) pushes the neutral material out of the system. This obscuring cloud is larger than the BLR and torus and covers a significant fraction of both. A region at the approximate distance to the torus remains unobscured; this is where the photoionized emission originates from. The exact nature and location of the consistent continuum component are unknown; we have placed it near the CIE because the data allows (but does not require) both components to be absorbed by the same neutral material.

Based on the work of Ishibashi et al. (2018), we expect the absorbing material to expand (blow-out) such that the continuum starts to overwhelm any collisionally ionized material that may be present within a few hundred thousand years. The criteria for this is the time it takes for an absorber with a column density of $\log N_{\text{H}} = 24 \text{ cm}^{-2}$ to expand and reach $\log N_{\text{H}} = 22.5 - 22.75 \text{ cm}^{-2}$. At these column densities, we would not expect to see the peculiar soft band behaviour that Mrk 1239 exhibits. If the AGN started with a lower column density, or if radiation pressure were able to preferentially blow out a section of the absorber such that the total covering fraction was reduced, then this time may be shorter. We expect the AGN duty cycle to last $\sim 10^7 - 10^8$ years

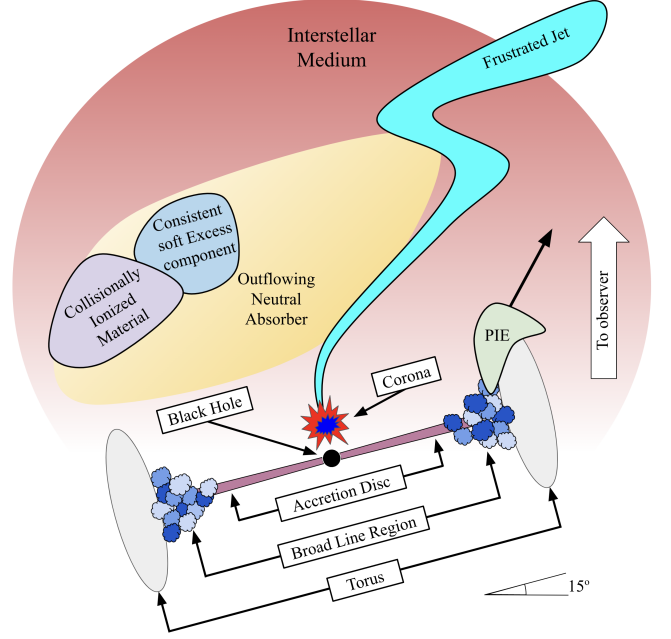


Figure 15. A possible profile view of the central engine in Mrk 1239. The standard components of an AGN are labelled, e.g. torus, broad line region, accretion disc, black hole and corona. The larger red corona is in the high state, while the smaller blue corona represents the low state. The corona is the base of a vertically extended jet (cyan) that pushes material to the neutral absorber. This absorber represents the 10^{23} cm^{-2} absorber that obscures the continuum emission from Mrk 1239. The outflowing neutral absorber crashes into the ISM (red), producing the collisionally ionized and possibly the constant continuum component. The photoionized material (PIE) is located on the other side of the central engine, where there may be a clear line of sight at torus-like distances.

(Parma et al. 2007). Assuming a duty cycle of 50 Myr and a blow-out time of 100 kyr, then it would take ~ 0.2 percent of an AGN active time to blow an absorber out such that it no longer displayed the collisionally ionized plasma features like Mrk 1239 possesses. Perhaps Mrk 1239 is preferentially blowing the material from one side, and this is what is creating the asymmetric nature of the absorbing cloud (see Figure 15). If the absorbing cloud has been preferentially removed at one side of the torus, then this could also be a possible explanation as to why the photoionized emitter is outflow.

This indicates that observing a type 1 Seyfert galaxy with this level of absorption is a rather rare event. Of the more than 800 Seyfert galaxies in the *Swift*-105 month survey (Oh et al. 2018), perhaps two share the unique timing and spectral properties that Mrk 1239 exhibits. The challenge of identifying these objects is that it is not just that they are short-lived and few in number but that they require careful timing and spectral analysis to identify. Sample searches in the *Swift*-LXSPS catalogue (Evans et al. 2023) and *eROSITA* (Predehl et al. 2021; Merloni et al. 2024) may be able to identify more of these objects.

7. CONCLUSIONS

We have revealed the behaviour of the central engine in new detail with the broadband long-term monitoring of Mrk 1239. We perform timing analysis on long-term (*Swift* data) and rapid (PN and *NuSTAR* data) time scales. We performed broadband X-ray spectral modelling with flux-resolved CCD spectra and compared our results to archival data of Mrk 1239, finding good agreement.

- The timing analysis of Mrk 1239, including the two *Swift* monitoring campaigns, shows that the central engine of Mrk 1239 is totally obscured by an $N_{\text{H}} \sim 10^{23} \text{ cm}^{-2}$ absorber. No central engine continuum variations are detected below 3 keV. Instead, the soft band emission originates on a larger physical scale. It is comprised of three main components: a collisionally ionized, photoionized, and a constant continuum component shaped similar to bremsstrahlung emission. The collisionally ionized and constant continuum components could be associated with a large-scale outflow crashing into the ISM, While the photoionized component is most likely related to the material at tours-like distances that have been photoionized by the unabsorbed primary continuum of Mrk 1239.
- The collisionally ionized plasma requires some absorption. Consequently, a star forming region is no longer favoured because it would require very high rates inconsistent with other measurements. Instead, we conclude that this region is consistent with outflowing material crashing into the ISM.
- The large amplitude, rapid flaring event seen in the data up to 30 keV can be attributed to a brightening of the primary continuum and not due to obscuration. In

combination with the presence of a Compton hump, a blurred reflection origin for the primary continuum is favoured.

- The accretion disc of Mrk 1239 is viewed virtually face-on, and it produces a strong reflection spectrum. The flaring event observed in Mrk 1239 was due to changes in the corona that propagated to changes in the accretion disc. The measured emissivity profile is consistent with a vertically extended primary source at large distance, possibly indicating that the base of the jet is serving as the corona.

We estimate less than 1 percent of AGN may have geometries similar to Mrk 1239. However, Mrk 1239 might be revealing a stage of rapid evolution in all AGN when the central region is being cleared of dense material and exposing the central engine. Further study is required to examine this type of galaxy.

- 1 We thank the referee for their helpful comments that improved this manuscript. This work was based on observations
- 2 obtained with XMM-Newton, an ESA science mission with
- 3 instruments and contributions directly funded by ESA Member
- 4 States and NASA. LCG acknowledges financial support
- 5 from the Natural Sciences and Engineering Research Council
- 6 of Canada (NSERC) and the Canadian Space Agency
- 7 (CSA). JJ acknowledges support from the Leverhulme Trust,
- 8 the Isaac Newton Trust, and St. Edmund's College University
- 9 of Cambridge.
- 10

DATA AVAILABILITY

All data are publicly available through the HEASARC archive.

REFERENCES

- Akaike, H. 1974, *IEEE Transactions on Automatic Control*, 19, 716
- Antonucci, R. 1993, *ARA&A*, 31, 473, doi: [10.1146/annurev.aa.31.090193.002353](https://doi.org/10.1146/annurev.aa.31.090193.002353)
- Arnaud, K. A. 1996, in *Astronomical Society of the Pacific Conference Series*, Vol. 101, *Astronomical Data Analysis Software and Systems V*, ed. G. H. Jacoby & J. Barnes, 17
- Ballantyne, D. R., Ross, R. R., & Fabian, A. C. 2001, *MNRAS*, 327, 10, doi: [10.1046/j.1365-8711.2001.04432.x](https://doi.org/10.1046/j.1365-8711.2001.04432.x)
- Batcheldor, D., Robinson, A., Axon, D. J., et al. 2011, *The Astrophysical Journal*, 738, 90, doi: [10.1088/0004-637X/738/1/90](https://doi.org/10.1088/0004-637X/738/1/90)
- Berton, M., Foschini, L., Ciroi, S., et al. 2015, *A&A*, 578, A28, doi: [10.1051/0004-6361/201525691](https://doi.org/10.1051/0004-6361/201525691)
- Berton, M., Congiu, E., Järvelä, E., et al. 2018, *A&A*, 614, A87, doi: [10.1051/0004-6361/201832612](https://doi.org/10.1051/0004-6361/201832612)
- Böhringer, H., & Werner, N. 2010, *A&A Rv*, 18, 127, doi: [10.1007/s00159-009-0023-3](https://doi.org/10.1007/s00159-009-0023-3)
- Boller, T., Brandt, W. N., & Fink, H. 1996, *AAP*, 305, 53, <https://arxiv.org/abs/astro-ph/9504093>
- Bonson, K., & Gallo, L. C. 2016, *MNRAS*, 458, 1927, doi: [10.1093/mnras/stw466](https://doi.org/10.1093/mnras/stw466)
- Boroson, B., Kim, D.-W., & Fabbiano, G. 2011, *ApJ*, 729, 12, doi: [10.1088/0004-637X/729/1/12](https://doi.org/10.1088/0004-637X/729/1/12)
- Brandt, W. N., Mathur, S., & Elvis, M. 1997, *MNRAS*, 285, L25, doi: [10.1093/mnras/285.3.L25](https://doi.org/10.1093/mnras/285.3.L25)
- Brenneman, L. W., & Reynolds, C. S. 2006, *ApJ*, 652, 1028, doi: [10.1086/508146](https://doi.org/10.1086/508146)

- Buhariwalla, M. Z., Gallo, L. C., Mao, J., et al. 2023, MNRAS, 521, 2378, doi: [10.1093/mnras/stad265](https://doi.org/10.1093/mnras/stad265)
- Buhariwalla, M. Z., Waddell, S. G. H., Gallo, L. C., Grupe, D., & Komossa, S. 2020, ApJ, 901, 118, doi: [10.3847/1538-4357/abb08a](https://doi.org/10.3847/1538-4357/abb08a)
- Burrows, D. N., Hill, J. E., Nousek, J. A., et al. 2004, in Society of Photo-Optical Instrumentation Engineers (SPIE) Conference Series, Vol. 5165, X-Ray and Gamma-Ray Instrumentation for Astronomy XIII, ed. K. A. Flanagan & O. H. W. Siegmund, 201–216, doi: [10.1117/12.504868](https://doi.org/10.1117/12.504868)
- Cash, W. 1979, ApJ, 228, 939, doi: [10.1086/156922](https://doi.org/10.1086/156922)
- Chiang, C.-Y., Walton, D. J., Fabian, A. C., Wilkins, D. R., & Gallo, L. C. 2015, MNRAS, 446, 759, doi: [10.1093/mnras/stu2087](https://doi.org/10.1093/mnras/stu2087)
- Choudhury, K., García, J. A., Steiner, J. F., & Bambi, C. 2017, ApJ, 851, 57, doi: [10.3847/1538-4357/aa9925](https://doi.org/10.3847/1538-4357/aa9925)
- Crenshaw, D. M., Kraemer, S. B., & George, I. M. 2003, ARA&A, 41, 117, doi: [10.1146/annurev.astro.41.082801.100328](https://doi.org/10.1146/annurev.astro.41.082801.100328)
- Dauser, T., Garcia, J., Wilms, J., et al. 2013, Monthly Notices of the Royal Astronomical Society, 430, 1694, doi: [10.1093/mnras/sts710](https://doi.org/10.1093/mnras/sts710)
- Dauser, T., García, J. A., Joyce, A., et al. 2022, Monthly Notices of the Royal Astronomical Society, 514, 3965, doi: [10.1093/mnras/stac1593](https://doi.org/10.1093/mnras/stac1593)
- Diehl, S., & Statler, T. S. 2007, ApJ, 668, 150, doi: [10.1086/521009](https://doi.org/10.1086/521009)
- Doi, A., Asada, K., Fujisawa, K., et al. 2013, The Astrophysical Journal, 765, 69, doi: [10.1088/0004-637x/765/1/69](https://doi.org/10.1088/0004-637x/765/1/69)
- Doi, A., Wajima, K., Hagiwara, Y., & Inoue, M. 2015, ApJL, 798, L30, doi: [10.1088/2041-8205/798/2/L30](https://doi.org/10.1088/2041-8205/798/2/L30)
- Edelson, R., Turner, T. J., Pounds, K., et al. 2002, ApJ, 568, 610, doi: [10.1086/323779](https://doi.org/10.1086/323779)
- Evans, P. A., Page, K. L., Beardmore, A. P., et al. 2023, MNRAS, 518, 174, doi: [10.1093/mnras/stac2937](https://doi.org/10.1093/mnras/stac2937)
- Evans, P. A., Beardmore, A. P., Page, K. L., et al. 2009, MNRAS, 397, 1177, doi: [10.1111/j.1365-2966.2009.14913.x](https://doi.org/10.1111/j.1365-2966.2009.14913.x)
- Fabbiano, G. 2012, The Hot ISM of Elliptical Galaxies: A Brief History (New York, NY: Springer New York), 1–19, doi: [10.1007/978-1-4614-0580-1_1](https://doi.org/10.1007/978-1-4614-0580-1_1)
- Fabian, A. C. 2012, ARA&A, 50, 455, doi: [10.1146/annurev-astro-081811-125521](https://doi.org/10.1146/annurev-astro-081811-125521)
- Fabian, A. C., Lohfink, A., Kara, E., et al. 2015, MNRAS, 451, 4375, doi: [10.1093/mnras/stv1218](https://doi.org/10.1093/mnras/stv1218)
- Fabian, A. C., Vasudevan, R. V., Mushotzky, R. F., Winter, L. M., & Reynolds, C. S. 2009a, MNRAS, 394, L89, doi: [10.1111/j.1745-3933.2009.00617.x](https://doi.org/10.1111/j.1745-3933.2009.00617.x)
- Fabian, A. C., Zoghbi, A., Ross, R. R., et al. 2009b, Nature, 459, 540, doi: [10.1038/nature08007](https://doi.org/10.1038/nature08007)
- Fabian, A. C., Zoghbi, A., Wilkins, D., et al. 2012, MNRAS, 419, 116, doi: [10.1111/j.1365-2966.2011.19676.x](https://doi.org/10.1111/j.1365-2966.2011.19676.x)
- Fanaroff, B. L., & Riley, J. M. 1974, MNRAS, 167, 31P, doi: [10.1093/mnras/167.1.31P](https://doi.org/10.1093/mnras/167.1.31P)
- Fanti, R., Fanti, C., Schilizzi, R. T., et al. 1990, A&A, 231, 333
- Feltre, A., Gruppioni, C., Marchetti, L., et al. 2023, A&A, 675, A74, doi: [10.1051/0004-6361/202245516](https://doi.org/10.1051/0004-6361/202245516)
- Foschini, L., Angelakis, E., Fuhrmann, L., et al. 2012, A&A, 548, A106, doi: [10.1051/0004-6361/201220225](https://doi.org/10.1051/0004-6361/201220225)
- Franceschini, A., Braito, V., Persic, M., et al. 2003, MNRAS, 343, 1181, doi: [10.1046/j.1365-8711.2003.06744.x](https://doi.org/10.1046/j.1365-8711.2003.06744.x)
- Gallo, L. 2018, PoS, NLS1-2018, 034, doi: [10.22323/1.328.0034](https://doi.org/10.22323/1.328.0034)
- Gallo, L. C., Gonzalez, A. G., & Miller, J. M. 2021, ApJL, 908, L33, doi: [10.3847/2041-8213/abdcbb](https://doi.org/10.3847/2041-8213/abdcbb)
- Gallo, L. C., Miller, J. M., & Costantini, E. 2023, arXiv e-prints, arXiv:2302.10930, doi: [10.48550/arXiv.2302.10930](https://doi.org/10.48550/arXiv.2302.10930)
- Gallo, L. C., Fabian, A. C., Grupe, D., et al. 2013, MNRAS, 428, 1191, doi: [10.1093/mnras/sts102](https://doi.org/10.1093/mnras/sts102)
- Gallo, L. C., Wilkins, D. R., Bonson, K., et al. 2015, MNRAS, 446, 633, doi: [10.1093/mnras/stu2108](https://doi.org/10.1093/mnras/stu2108)
- García, J., Dauser, T., Reynolds, C. S., et al. 2013, ApJ, 768, 146, doi: [10.1088/0004-637X/768/2/146](https://doi.org/10.1088/0004-637X/768/2/146)
- García, J., & Kallman, T. R. 2010, ApJ, 718, 695, doi: [10.1088/0004-637X/718/2/695](https://doi.org/10.1088/0004-637X/718/2/695)
- García, J., Dauser, T., Lohfink, A., et al. 2014, ApJ, 782, 76, doi: [10.1088/0004-637X/782/2/76](https://doi.org/10.1088/0004-637X/782/2/76)
- George, I. M., & Fabian, A. C. 1991, MNRAS, 249, 352, doi: [10.1093/mnras/249.2.352](https://doi.org/10.1093/mnras/249.2.352)
- Gierliński, M., & Done, C. 2004, MNRAS, 349, L7, doi: [10.1111/j.1365-2966.2004.07687.x](https://doi.org/10.1111/j.1365-2966.2004.07687.x)
- Gonzalez, A. G., Wilkins, D. R., & Gallo, L. C. 2017, MNRAS, 472, 1932, doi: [10.1093/mnras/stx2080](https://doi.org/10.1093/mnras/stx2080)
- Goodrich, R. W. 1989, ApJ, 342, 224, doi: [10.1086/167586](https://doi.org/10.1086/167586)
- Grafton-Waters, S., Mao, J., Mehdipour, M., et al. 2023, A&A, 673, A26, doi: [10.1051/0004-6361/202243681](https://doi.org/10.1051/0004-6361/202243681)
- Gravity Collaboration, Amorim, A., Bourdarot, G., et al. 2023, A&A, 669, A14, doi: [10.1051/0004-6361/202244655](https://doi.org/10.1051/0004-6361/202244655)
- GRAVITY Collaboration, Amorim, A., Bourdarot, G., et al. 2024, arXiv e-prints, arXiv:2401.07676, doi: [10.48550/arXiv.2401.07676](https://doi.org/10.48550/arXiv.2401.07676)
- Grupe, D. 1996, PhD thesis, -
- Grupe, D. 2004, The Astronomical Journal, 127, 1799, doi: [10.1086/382516](https://doi.org/10.1086/382516)
- Grupe, D., Beuermann, K., Thomas, H. C., Mannheim, K., & Fink, H. H. 1998, A&A, 330, 25, <https://arxiv.org/abs/astro-ph/9710298>
- Grupe, D., Mathur, S., & Komossa, S. 2004, AJ, 127, 3161, doi: [10.1086/421002](https://doi.org/10.1086/421002)
- Gruppioni, C., Berta, S., Spinoglio, L., et al. 2016, MNRAS, 458, 4297, doi: [10.1093/mnras/stw577](https://doi.org/10.1093/mnras/stw577)
- Gültekin, K., Richstone, D. O., Gebhardt, K., et al. 2009, ApJ, 698, 198, doi: [10.1088/0004-637X/698/1/198](https://doi.org/10.1088/0004-637X/698/1/198)

- Haardt, F., & Maraschi, L. 1993, *ApJ*, 413, 507, doi: [10.1086/173020](https://doi.org/10.1086/173020)
- Harrison, F. A., Craig, W. W., Christensen, F. E., et al. 2013, *ApJ*, 770, 103, doi: [10.1088/0004-637X/770/2/103](https://doi.org/10.1088/0004-637X/770/2/103)
- Hickox, R. C., & Alexander, D. M. 2018, *ARA&A*, 56, 625, doi: [10.1146/annurev-astro-081817-051803](https://doi.org/10.1146/annurev-astro-081817-051803)
- Holt, S. S., Mushotzky, R. F., Becker, R. H., et al. 1980, *ApJL*, 241, L13, doi: [10.1086/183350](https://doi.org/10.1086/183350)
- Husemann, B., Singha, M., Scharwächter, J., et al. 2022, *A&A*, 659, A124, doi: [10.1051/0004-6361/202141312](https://doi.org/10.1051/0004-6361/202141312)
- Ishibashi, W., Fabian, A. C., Ricci, C., & Celotti, A. 2018, *MNRAS*, 479, 3335, doi: [10.1093/mnras/sty1620](https://doi.org/10.1093/mnras/sty1620)
- Ivezić, Ž., Connolly, A. J., Vanderplas, J. T., & Gray, A. 2019, *Statistics, Data Mining, and Machine Learning in Astronomy*
- Jansen, F., Lumb, D., Altieri, B., et al. 2001, *AAP*, 365, L1, doi: [10.1051/0004-6361:20000036](https://doi.org/10.1051/0004-6361:20000036)
- Järvelä, E., Dahale, R., Crepaldi, L., et al. 2022, *A&A*, 658, A12, doi: [10.1051/0004-6361/202141698](https://doi.org/10.1051/0004-6361/202141698)
- Jiang, J., Baloković, M., Brightman, M., et al. 2021, *MNRAS*, 505, 702, doi: [10.1093/mnras/stab1306](https://doi.org/10.1093/mnras/stab1306)
- Jiang, J., Fabian, A. C., Dauser, T., et al. 2019, *MNRAS*, 489, 3436, doi: [10.1093/mnras/stz2326](https://doi.org/10.1093/mnras/stz2326)
- Jun, H. D., Assef, R. J., Carroll, C. M., et al. 2021, *ApJ*, 906, 21, doi: [10.3847/1538-4357/abc629](https://doi.org/10.3847/1538-4357/abc629)
- Kaastra, J. S., & Bleeker, J. A. M. 2016, *A&A*, 587, A151, doi: [10.1051/0004-6361/201527395](https://doi.org/10.1051/0004-6361/201527395)
- Kallman, T., & Bautista, M. 2001, *ApJS*, 133, 221, doi: [10.1086/319184](https://doi.org/10.1086/319184)
- Kammoun, E. S., Nardini, E., & Risaliti, G. 2018, *A&A*, 614, A44, doi: [10.1051/0004-6361/201732377](https://doi.org/10.1051/0004-6361/201732377)
- Karzas, W. J., & Latter, R. 1961, *ApJS*, 6, 167, doi: [10.1086/190063](https://doi.org/10.1086/190063)
- Kellogg, E., Baldwin, J. R., & Koch, D. 1975, *ApJ*, 199, 299, doi: [10.1086/153692](https://doi.org/10.1086/153692)
- Komossa, S. 2008, in *Rev. Mex. Astron. Astrofis. Conference Series*, Vol. 32, *Rev. Mex. Astron. Astrofis. Conference Series*, 86–92. <https://arxiv.org/abs/0710.3326>
- Komossa, S., Voges, W., Xu, D., et al. 2006, *AJ*, 132, 531, doi: [10.1086/505043](https://doi.org/10.1086/505043)
- König, S., Eckart, A., García-Marín, M., & Huchtmeier, W. K. 2009, *A&A*, 507, 757, doi: [10.1051/0004-6361/200912546](https://doi.org/10.1051/0004-6361/200912546)
- Koshida, S., Minezaki, T., Yoshii, Y., et al. 2014, *The Astrophysical Journal*, 788, 159, doi: [10.1088/0004-637X/788/2/159](https://doi.org/10.1088/0004-637X/788/2/159)
- Kunert-Bajraszewska, M., Gawroński, M. P., Labiano, A., & Siemiginowska, A. 2010, *MNRAS*, 408, 2261, doi: [10.1111/j.1365-2966.2010.17271.x](https://doi.org/10.1111/j.1365-2966.2010.17271.x)
- Lakićević, M., Kovačević-Dojčinović, J., & Popović, L. Č. 2022, *MNRAS*, 509, 831, doi: [10.1093/mnras/stab2926](https://doi.org/10.1093/mnras/stab2926)
- Laor, A. 1991, *ApJ*, 376, 90, doi: [10.1086/170257](https://doi.org/10.1086/170257)
- Leighly, K. M. 1999a, *ApJS*, 125, 297, doi: [10.1086/313277](https://doi.org/10.1086/313277)
- . 1999b, *ApJs*, 125, 317, doi: [10.1086/313287](https://doi.org/10.1086/313287)
- Liddle, A. R. 2007, *Monthly Notices of the Royal Astronomical Society: Letters*, 377, L74, doi: [10.1111/j.1745-3933.2007.00306.x](https://doi.org/10.1111/j.1745-3933.2007.00306.x)
- Longair, M. S. 1992, *High energy astrophysics. Vol.1: Particles, photons and their detection* (Cambridge University Press)
- Madsen, K. K., Grefenstette, B. W., Pike, S., et al. 2020, *arXiv e-prints*, arXiv:2005.00569, doi: [10.48550/arXiv.2005.00569](https://doi.org/10.48550/arXiv.2005.00569)
- Madsen, K. K., Harrison, F. A., Markwardt, C. B., et al. 2015, *ApJS*, 220, 8, doi: [10.1088/0067-0049/220/1/8](https://doi.org/10.1088/0067-0049/220/1/8)
- Magdziarz, P., Blaes, O. M., Zdziarski, A. A., Johnson, W. N., & Smith, D. A. 1998, *MNRAS*, 301, 179, doi: [10.1046/j.1365-8711.1998.02015.x](https://doi.org/10.1046/j.1365-8711.1998.02015.x)
- Magdziarz, P., & Zdziarski, A. A. 1995, *MNRAS*, 273, 837, doi: [10.1093/mnras/273.3.837](https://doi.org/10.1093/mnras/273.3.837)
- Marin, F. 2016, *MNRAS*, 460, 3679, doi: [10.1093/mnras/stw1131](https://doi.org/10.1093/mnras/stw1131)
- Mathews, W. G. 2021, *MNRAS*, 506, 2030, doi: [10.1093/mnras/stab1745](https://doi.org/10.1093/mnras/stab1745)
- Mathur, S. 2000, *MNRAS*, 314, L17, doi: [10.1046/j.1365-8711.2000.03530.x](https://doi.org/10.1046/j.1365-8711.2000.03530.x)
- Matsushita, K., Makishima, K., Ikebe, Y., et al. 1998, *The Astrophysical Journal*, 499, L13, doi: [10.1086/311339](https://doi.org/10.1086/311339)
- Mazzarella, J. M., & Balzano, V. A. 1986, *ApJS*, 62, 751, doi: [10.1086/191155](https://doi.org/10.1086/191155)
- Merloni, A., Lamer, G., Liu, T., et al. 2024, *arXiv e-prints*, arXiv:2401.17274, doi: [10.48550/arXiv.2401.17274](https://doi.org/10.48550/arXiv.2401.17274)
- Minezaki, T., Yoshii, Y., Kobayashi, Y., et al. 2019, *ApJ*, 886, 150, doi: [10.3847/1538-4357/ab4f7b](https://doi.org/10.3847/1538-4357/ab4f7b)
- Miniutti, G., & Fabian, A. C. 2004, *MNRAS*, 349, 1435, doi: [10.1111/j.1365-2966.2004.07611.x](https://doi.org/10.1111/j.1365-2966.2004.07611.x)
- Morganti, R. 2017, *Frontiers in Astronomy and Space Sciences*, 4, doi: [10.3389/fspas.2017.00042](https://doi.org/10.3389/fspas.2017.00042)
- Nandra, K., George, I. M., Mushotzky, R. F., Turner, T. J., & Yaqoob, T. 1997, *ApJ*, 477, 602, doi: [10.1086/303721](https://doi.org/10.1086/303721)
- Nandra, K., Barret, D., Barcons, X., et al. 2013, *arXiv e-prints*, arXiv:1306.2307, doi: [10.48550/arXiv.1306.2307](https://doi.org/10.48550/arXiv.1306.2307)
- Netzer, H. 2013, *The Physics and Evolution of Active Galactic Nuclei*. (Cambridge University Press). <https://search.ebscohost.com/login.aspx?direct=true&db=nlebk&AN=527870&site=ehost-live>
- O’Dea, C. P. 1998, *PASP*, 110, 493, doi: [10.1086/316162](https://doi.org/10.1086/316162)
- Oh, K., Koss, M., Markwardt, C. B., et al. 2018, *ApJS*, 235, 4, doi: [10.3847/1538-4365/aaa7fd](https://doi.org/10.3847/1538-4365/aaa7fd)
- Osterbrock, D. E., & Pogge, R. W. 1985, *ApJ*, 297, 166, doi: [10.1086/163513](https://doi.org/10.1086/163513)
- Pan, X., Lu, H., Komossa, S., et al. 2019, *ApJ*, 870, 75, doi: [10.3847/1538-4357/aaf1bc](https://doi.org/10.3847/1538-4357/aaf1bc)
- Pan, X., Zhou, H., Yang, C., et al. 2021, *ApJ*, 912, 118, doi: [10.3847/1538-4357/abf148](https://doi.org/10.3847/1538-4357/abf148)

- Park, T., Kashyap, V. L., Siemiginowska, A., et al. 2006, *ApJ*, 652, 610, doi: [10.1086/507406](https://doi.org/10.1086/507406)
- Parker, M. L., Marinucci, A., Brenneman, L., et al. 2013, *Monthly Notices of the Royal Astronomical Society*, 437, 721, doi: [10.1093/mnras/stt1925](https://doi.org/10.1093/mnras/stt1925)
- Parker, M. L., Walton, D. J., Fabian, A. C., & Risaliti, G. 2014, *MNRAS*, 441, 1817, doi: [10.1093/mnras/stu712](https://doi.org/10.1093/mnras/stu712)
- Parma, P., Murgia, M., de Ruiter, H. R., et al. 2007, *A&A*, 470, 875, doi: [10.1051/0004-6361:20077592](https://doi.org/10.1051/0004-6361:20077592)
- Peterson, B. M. 1997, *An Introduction to Active Galactic Nuclei* (Cambridge University Press)
- Peterson, B. M., & Wandel, A. 1999, *ApJL*, 521, L95, doi: [10.1086/312190](https://doi.org/10.1086/312190)
- Peterson, B. M., Ferrarese, L., Gilbert, K. M., et al. 2004, *ApJ*, 613, 682, doi: [10.1086/423269](https://doi.org/10.1086/423269)
- Ponti, G., Papadakis, I., Bianchi, S., et al. 2012, *A&A*, 542, A83, doi: [10.1051/0004-6361/201118326](https://doi.org/10.1051/0004-6361/201118326)
- Pounds, K. A., Done, C., & Osborne, J. P. 1995, *MNRAS*, 277, L5, doi: [10.1093/mnras/277.1.L5](https://doi.org/10.1093/mnras/277.1.L5)
- Pounds, K. A., Nixon, C. J., Lobban, A., & King, A. R. 2018, *MNRAS*, 481, 1832, doi: [10.1093/mnras/sty2359](https://doi.org/10.1093/mnras/sty2359)
- Predehl, P., Andritschke, R., Arefiev, V., et al. 2021, *A&A*, 647, A1, doi: [10.1051/0004-6361/202039313](https://doi.org/10.1051/0004-6361/202039313)
- Puchnarewicz, E. M., Mason, K. O., Cordova, F. A., et al. 1992, *MNRAS*, 256, 589, doi: [10.1093/mnras/256.3.589](https://doi.org/10.1093/mnras/256.3.589)
- Ranalli, P., Comastri, A., & Setti, G. 2003, *A&A*, 399, 39, doi: [10.1051/0004-6361:20021600](https://doi.org/10.1051/0004-6361:20021600)
- Robertis, M. M. D., Hayhoe, K., & Yee, H. K. C. 1998, *The Astrophysical Journal Supplement Series*, 115, 163, doi: [10.1086/313089](https://doi.org/10.1086/313089)
- Rodríguez-Ardila, A., & Mazzalay, X. 2006, *MNRAS: Letters*, 367, L57, doi: [10.1111/j.1745-3933.2006.00139.x](https://doi.org/10.1111/j.1745-3933.2006.00139.x)
- Ross, R. R., & Fabian, A. C. 2005, *MNRAS*, 358, 211, doi: [10.1111/j.1365-2966.2005.08797.x](https://doi.org/10.1111/j.1365-2966.2005.08797.x)
- Ruschel-Dutra, D., Rodríguez Espinosa, J. M., González Martán, O., Pastoriza, M., & Riffel, R. 2016, *MNRAS*, 466, 3353, doi: [10.1093/mnras/stw3276](https://doi.org/10.1093/mnras/stw3276)
- Rybicki, G. B., & Lightman, A. P. 1979, *Radiative processes in astrophysics* (Wiley)
- Sani, E., Lutz, D., Risaliti, G., et al. 2010, *MNRAS*, 403, 1246, doi: [10.1111/j.1365-2966.2009.16217.x](https://doi.org/10.1111/j.1365-2966.2009.16217.x)
- Seyfert, C. K. 1943, *ApJ*, 97, 28, doi: [10.1086/144488](https://doi.org/10.1086/144488)
- Shakura, N. I., & Sunyaev, R. A. 1973, *A&A*, 500, 33
- Smirnova-Pinchukova, I., Husemann, B., Davis, T. A., et al. 2022, *A&A*, 659, A125, doi: [10.1051/0004-6361/202142011](https://doi.org/10.1051/0004-6361/202142011)
- Smith, R. K., Brickhouse, N. S., Liedahl, D. A., & Raymond, J. C. 2001, *ApJL*, 556, L91, doi: [10.1086/322992](https://doi.org/10.1086/322992)
- Smith, R. K., Abraham, M., Baird, G., et al. 2019, in *Society of Photo-Optical Instrumentation Engineers (SPIE) Conference Series*, Vol. 11118, *UV, X-Ray, and Gamma-Ray Space Instrumentation for Astronomy XXI*, ed. O. H. Siegmund, 111180W, doi: [10.1117/12.2529499](https://doi.org/10.1117/12.2529499)
- Sugiura, N. 1978, *Communications in Statistics - Theory and Methods*, 7, 13, doi: [10.1080/03610927808827599](https://doi.org/10.1080/03610927808827599)
- Tan, M. Y. J., & Biswas, R. 2012, *Monthly Notices of the Royal Astronomical Society*, 419, 3292, doi: [10.1111/j.1365-2966.2011.19969.x](https://doi.org/10.1111/j.1365-2966.2011.19969.x)
- Tanaka, Y., Boller, T., Gallo, L., Keil, R., & Ueda, Y. 2004, *PASJ*, 56, L9, doi: [10.1093/pasj/56.3.L9](https://doi.org/10.1093/pasj/56.3.L9)
- Tanaka, Y., Ueda, Y., & Boller, T. 2003, *MNRAS*, 338, L1, doi: [10.1046/j.1365-8711.2003.06110.x](https://doi.org/10.1046/j.1365-8711.2003.06110.x)
- Tanaka, Y., Nandra, K., Fabian, A. C., et al. 1995, *Nature*, 375, 659, doi: [10.1038/375659a0](https://doi.org/10.1038/375659a0)
- Urry, C. M., & Padovani, P. 1995, *PASP*, 107, 803, doi: [10.1086/133630](https://doi.org/10.1086/133630)
- Urry, M. 2003, in *Astronomical Society of the Pacific Conference Series*, Vol. 290, *Active Galactic Nuclei: From Central Engine to Host Galaxy*, ed. S. Collin, F. Combes, & I. Shlosman, 3, doi: [10.48550/arXiv.astro-ph/0301309](https://doi.org/10.48550/arXiv.astro-ph/0301309)
- Varglund, I., Järvelä, E., Lähteenmäki, A., et al. 2022, *A&A*, 668, A91, doi: [10.1051/0004-6361/202244465](https://doi.org/10.1051/0004-6361/202244465)
- Virtanen, P., Gommers, R., Oliphant, T. E., et al. 2020, *Nature Methods*, 17, 261, doi: [10.1038/s41592-019-0686-2](https://doi.org/10.1038/s41592-019-0686-2)
- Waddell, S. G. H., & Gallo, L. C. 2020, *MNRAS*, 498, 5207, doi: [10.1093/mnras/staa2783](https://doi.org/10.1093/mnras/staa2783)
- Waddell, S. G. H., Gallo, L. C., Gonzalez, A. G., Tripathi, S., & Zoghbi, A. 2019, *MNRAS*, 489, 5398, doi: [10.1093/mnras/stz2518](https://doi.org/10.1093/mnras/stz2518)
- Wilkins, D. R., & Fabian, A. C. 2012, *MNRAS*, 424, 1284, doi: [10.1111/j.1365-2966.2012.21308.x](https://doi.org/10.1111/j.1365-2966.2012.21308.x)
- Wilkins, D. R., & Gallo, L. C. 2015, *MNRAS*, 449, 129, doi: [10.1093/mnras/stv162](https://doi.org/10.1093/mnras/stv162)
- Wilkins, D. R., Gallo, L. C., Costantini, E., Brandt, W. N., & Blandford, R. D. 2022, *MNRAS*, 512, 761, doi: [10.1093/mnras/stac416](https://doi.org/10.1093/mnras/stac416)
- Wilkins, D. R., Kara, E., Fabian, A. C., & Gallo, L. C. 2014, *Monthly Notices of the Royal Astronomical Society*, 443, 2746, doi: [10.1093/mnras/stu1273](https://doi.org/10.1093/mnras/stu1273)
- Willingale, R., Starling, R. L. C., Beardmore, A. P., Tanvir, N. R., & O'Brien, P. T. 2013, *MNRAS*, 431, 394, doi: [10.1093/mnras/stt175](https://doi.org/10.1093/mnras/stt175)
- Wilms, J., Allen, A., & McCray, R. 2000, *ApJ*, 542, 914, doi: [10.1086/317016](https://doi.org/10.1086/317016)
- Xu, H., Kahn, S. M., Peterson, J. R., et al. 2002, *ApJ*, 579, 600, doi: [10.1086/342828](https://doi.org/10.1086/342828)
- Zhang, T.-Z., & Wu, X.-B. 2002, *ChJA&A*, 2, 487, doi: [10.1088/1009-9271/2/6/487](https://doi.org/10.1088/1009-9271/2/6/487)

Zoghbi, A., Fabian, A. C., Uttley, P., et al. 2010, MNRAS, 401,
2419, doi: [10.1111/j.1365-2966.2009.15816.x](https://doi.org/10.1111/j.1365-2966.2009.15816.x)

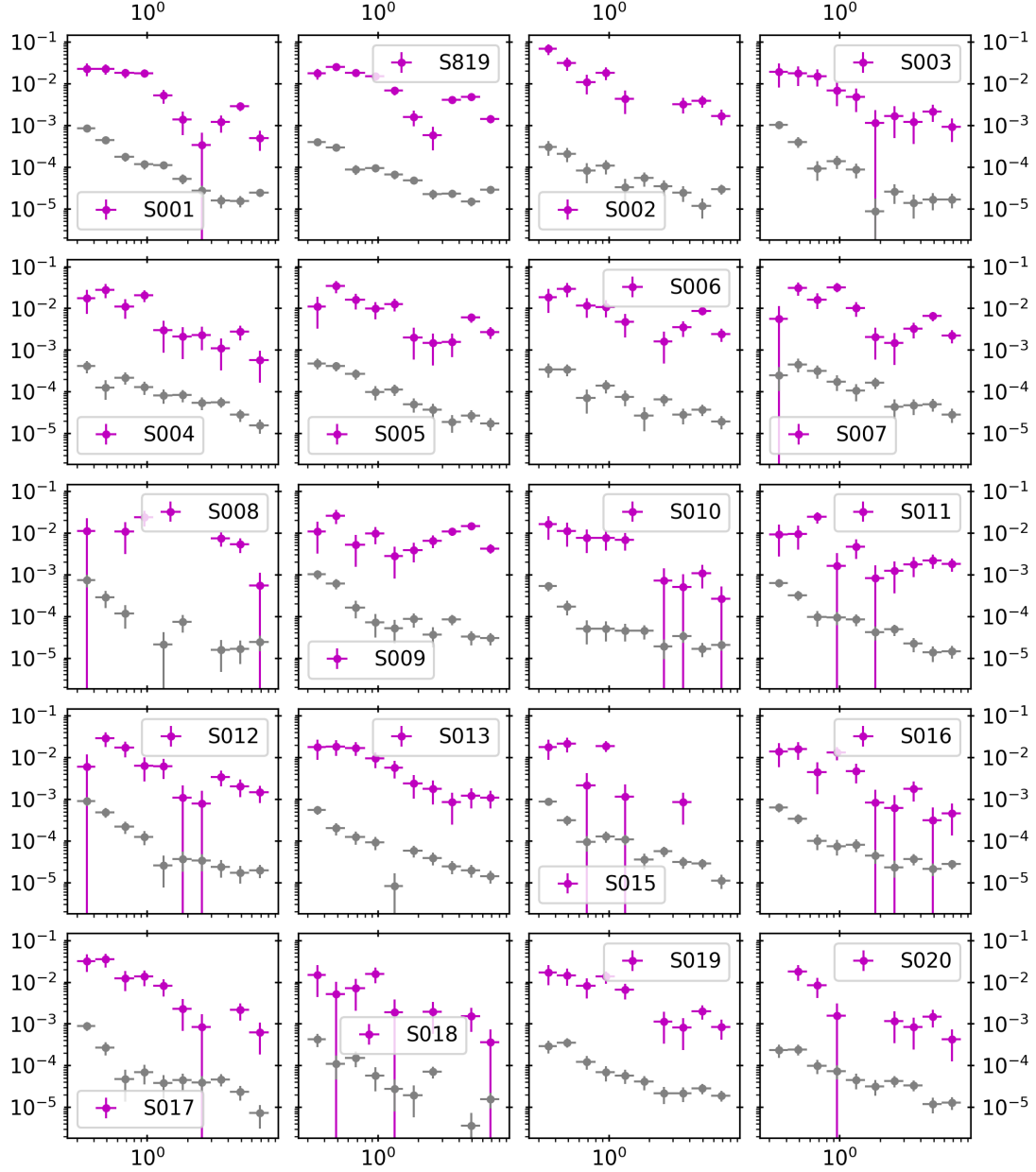


Figure 16. *Swift* spectrum for observations detailed in Table 2. The data has been binned into 10 bins to match the first principal component seen in Figure 6. The gray data represent the background for each *Swift* observation.

APPENDIX

A. *Swift* SPECTRAL DATA

B. SIMULATED PCA PRINCIPAL COMPONENT 1

C. SIMULATED PN DATA

D. MCMC CORNER PLOTS

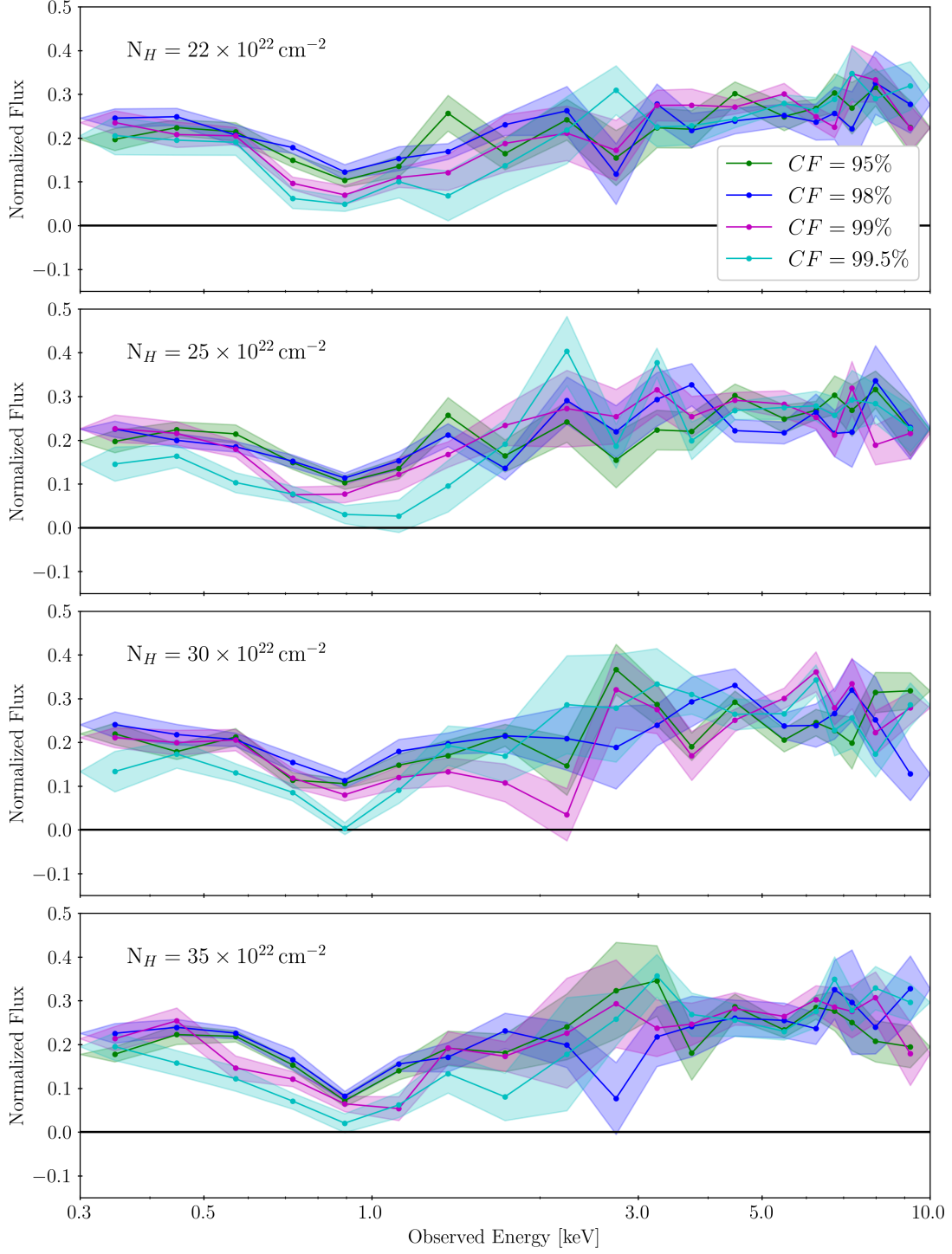


Figure 17. The first principal component for the sixteen simulated absorbers described in Section 3.5. The absorbers are grouped by column density, with the top panel showing those with $N_H = 22 \times 10^{22} \text{ cm}^{-2}$, the second panel showing those with $N_H = 25 \times 10^{22} \text{ cm}^{-2}$, the third panel showing those with $N_H = 30 \times 10^{22} \text{ cm}^{-2}$, and the forth panel showing those with $N_H = 35 \times 10^{22} \text{ cm}^{-2}$. Each panel has absorbers with covering fractions of $CF = 95, 98, 99$, and 99.5% . All simulated absorbers produced a first principal component that was inconsistent with the first principal component of the PN spectra.

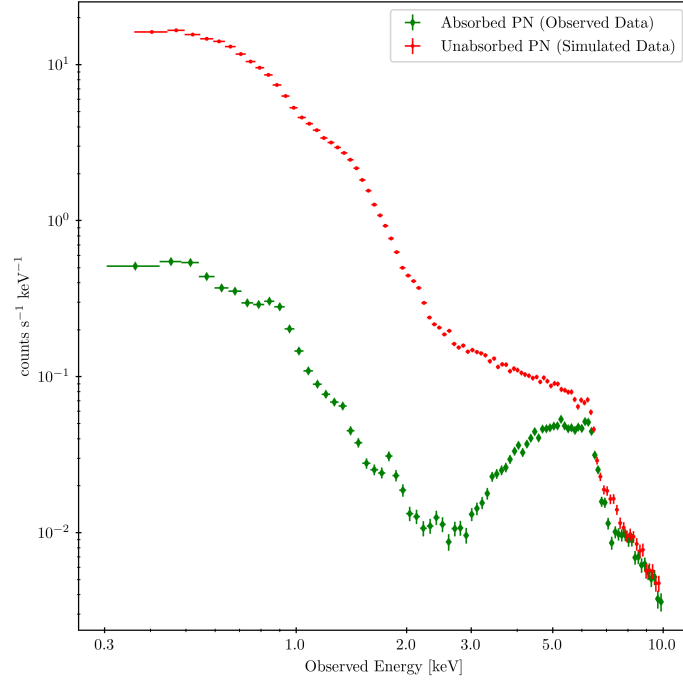


Figure 18. The observed PN spectra (green diamonds) compared to a simulated PN spectra based on the best fit low-state model with no absorption. See section 4.3 for details.

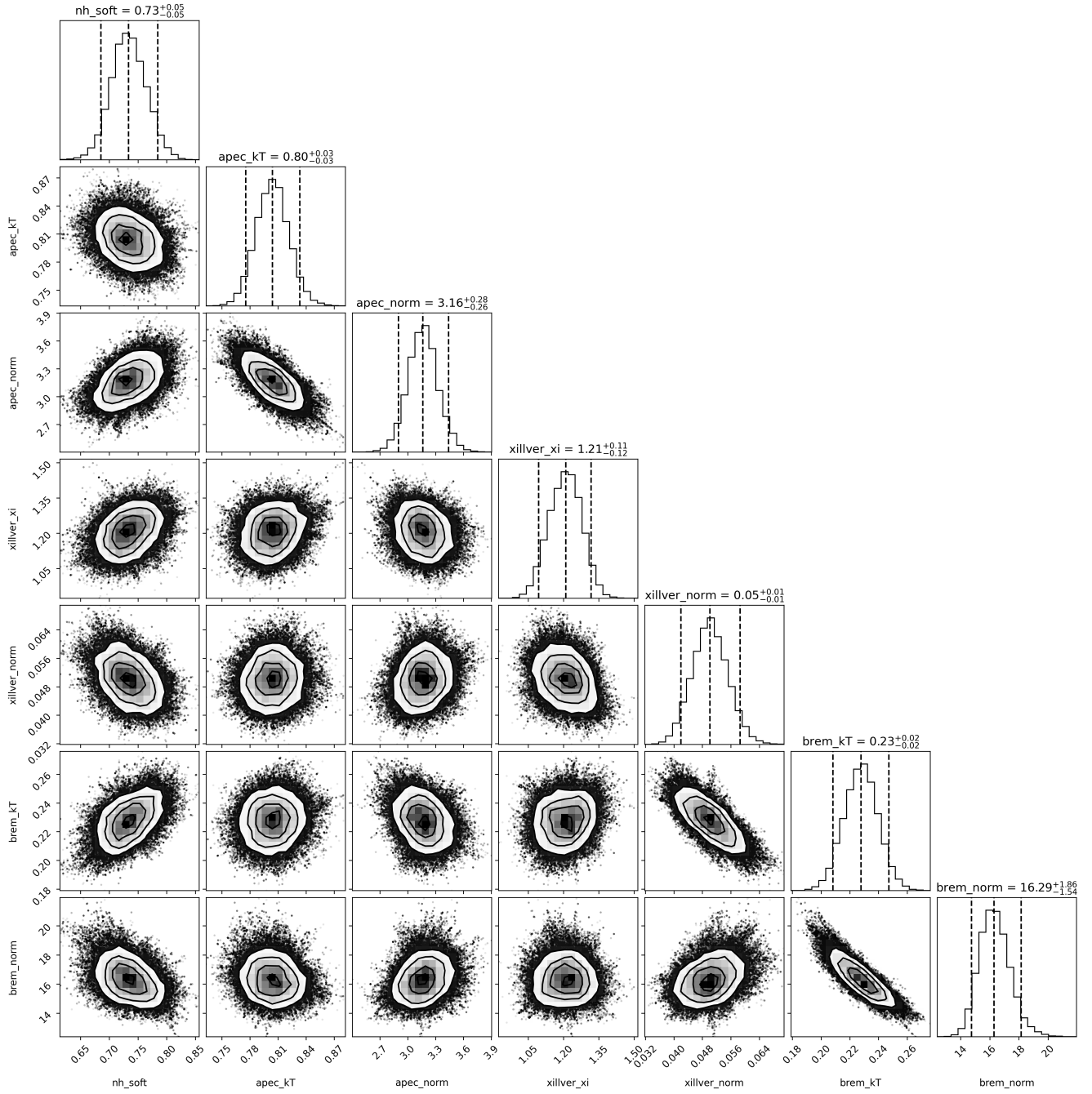


Figure 19. The corner plots for the MCMC best fit for the soft band components. Note that nh_soft is the column density of the absorber applied to the APEC component.

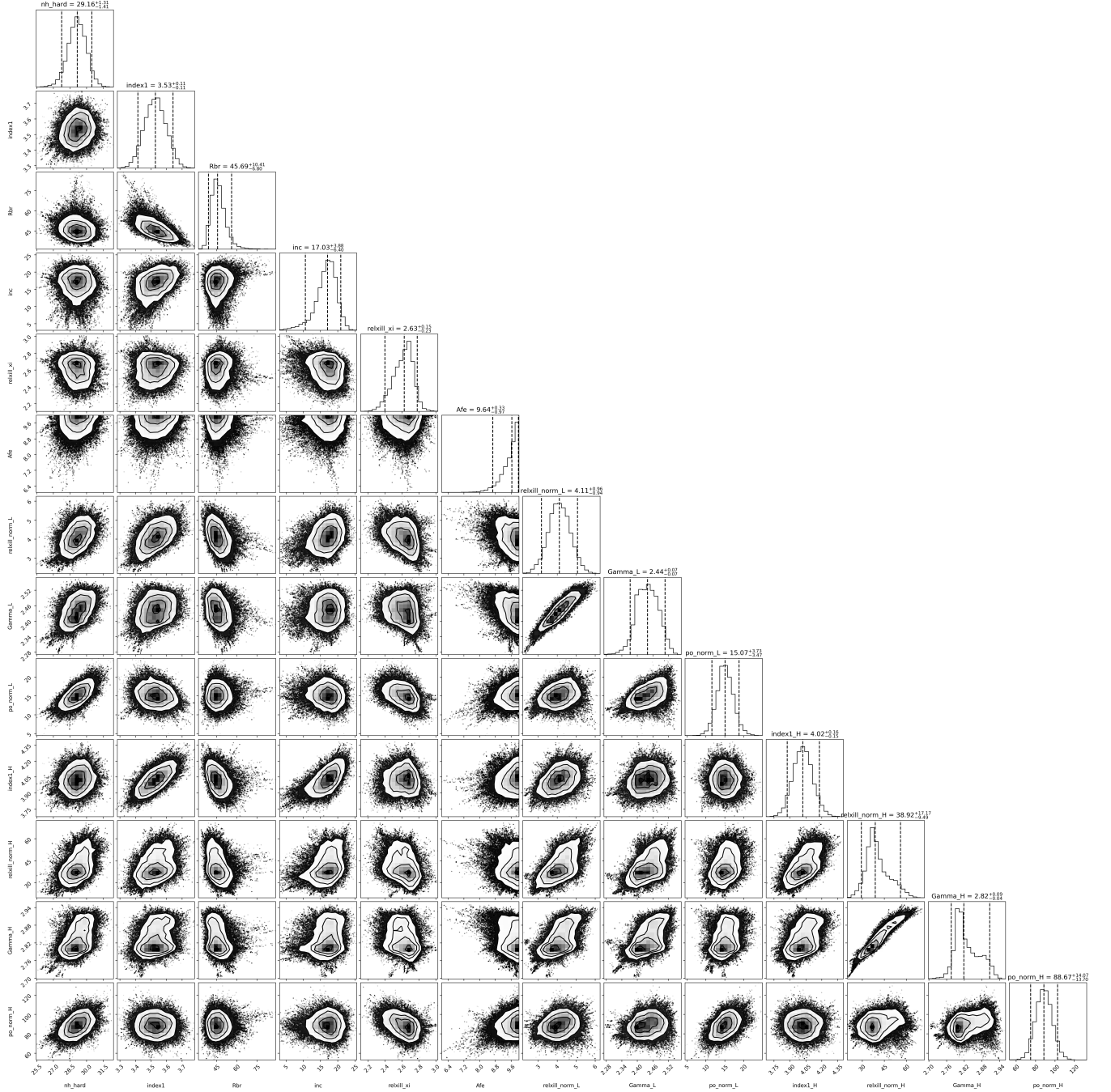


Figure 20. The corner plots for the MCMC best fit for the hard band components. Parameters that lack the subscript L or H denote values that were linked between epochs, while parameters with the subscript L indicate the low state value and parameters with subscript H indicate the high state value. Note that `nh_hard` is the column density of the absorber applied to the continuum components.

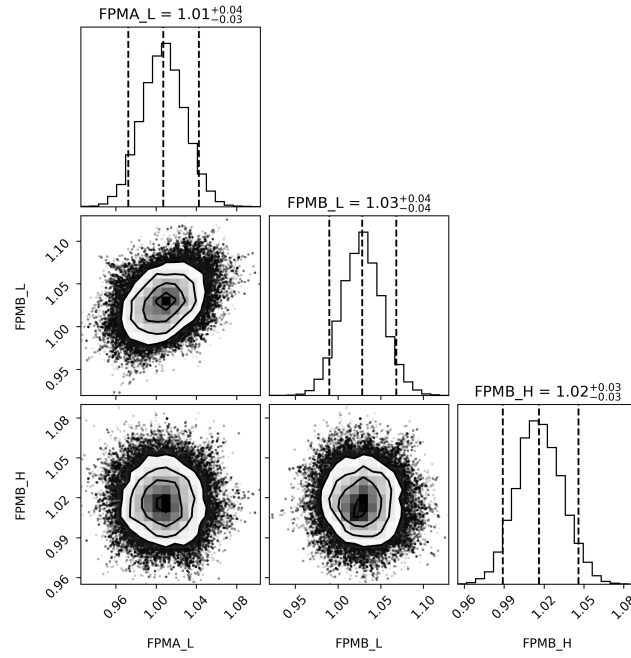


Figure 21. The corner plots for the MCMC best fit for the calibration constants. parameters with the subscript L indicate the low state calibration constants while the parameter with the subscript H indicates the high state calibration constant.